The Astrophysical Journal Supplement Series, 256:13 (27pp), 2021 September https://doi.org/10.3847/1538-4365/ac072a

Catalog of Long-term Transient Sources in the First 10 yr of Fermi-LAT Data

L. Baldini[1], J. Ballet[2], D. Bastieri[3,4], J. Becerra Gonzalez[5], R. Bellazzini[6], A. Berretta[7,8], E. Bissaldi[9,10], R. D. Blandford[11], E. D. Bloom[11], R. Bonino[12,13], E. Bottacini[11,14], P. Bruel[15], S. Buson[16], R. A. Cameron[11], P. A. Caraveo[17], E. Cavazzuti[18], S. Chen[3,14], G. Chiaro[17], D. Ciangottini[8], N. Cibario[12,13], S. Ciprini[19,20], P. Cristarella Orestano[7,8], M. Crnogorcevic[21], S. Cutini[8], F. D'Ammando[22], P. de la Torre Luque[9], F. de Palma[23,24], S. W. Digel[11], N. Di Lalla[11], F. Dirirsa[25], L. Di Venere[9,10], A. Domínguez[26], A. Fiori[27], H. Fleischhack[28,29,30], A. Franckowiak[31], Y. Fukazawa[32], S. Funk[33], P. Fusco[9,10], F. Gargano[10], D. Gasparrini[19,20], S. Germani[7,8], N. Giglietto[9,10], F. Giordano[9,10], M. Giroletti[22], D. Green[34], I. A. Grenier[2], S. Griffin[29], S. Guiriec[29,35], M. Gustafsson[36], J. W. Hewitt[37], D. Horan[15], R. Imazawa[32], G. Jóhannesson[38,39], M. Kerr[40], D. Kocevski[41], M. Kuss[6], S. Larsson[42,43,44], L. Latronico[12], J. Li[45], I. Liodakis[46], F. Longo[47,48], F. Loparco[9,10], M. N. Lovellette[40], P. Lubrano[8], S. Maldera[12], A. Manfreda[1], G. Martí-Devesa[49], H. Matake[32], M. N. Mazziotta[10], I. Mereu[8], M. Meyer[33], N. Mirabal[29,50], W. Mitthumsiri[51], T. Mizuno[52], M. E. Monzani[11], A. Morselli[19], I. V. Moskalenko[11], S. Nagasawa[53], M. Negro[30,50], R. Ojha[29], M. Orienti[22], E. Orlando[11,54], M. Palatiello[47,48,55], V. Paliya[45,56], D. Paneque[34], Z. Pei[4], M. Persic[47,57], M. Pesce-Rollins[6], V. Petrosian[11], H. Poon[32], T. A. Porter[11], G. Principe[22,47,48], J. L. Racusin[29], S. Rainò[9,10], R. Rando[3,14,58], B. Rani[29,59,60], M. Razzano[6,74], S. Razzaque[61], A. Reimer[11,49], O. Reimer[49], P. M. Saz Parkinson[62,63,64], L. Scotton[65], D. Serini[9], C. Sgrò[6], E. J. Siskind[66], G. Spandre[6], P. Spinelli[9,10], D. J. Suson[67], H. Tajima[11,68], D. Tak[29,69], D. F. Torres[70,71], G. Tosti[7,8], E. Troja[21,29], K. Wood[72], M. Yassine[47,48], and G. Zaharijas[54,73]

The Fermi-LAT Collaboration

[1] Università di Pisa and Istituto Nazionale di Fisica Nucleare, Sezione di Pisa I-56127 Pisa, Italy
[2] AIM, CEA, CNRS, Université Paris-Saclay, Université de Paris, F-91191 Gif-sur-Yvette, France
[3] Istituto Nazionale di Fisica Nucleare, Sezione di Padova, I-35131 Padova, Italy
[4] Dipartimento di Fisica e Astronomia "G. Galilei", Università di Padova, I-35131 Padova, Italy
[5] Instituto de Astrofísica de Canarias, Observatorio del Teide, C/Via Lactea, s/n, E-38205 La Laguna, Tenerife, Spain
[6] Istituto Nazionale di Fisica Nucleare, Sezione di Pisa, I-56127 Pisa, Italy
[7] Dipartimento di Fisica, Università degli Studi di Perugia, I-06123 Perugia, Italy; gino.tosti@unipg.it
[8] Istituto Nazionale di Fisica Nucleare, Sezione di Perugia, I-06123 Perugia, Italy; sara.cutini@pg.infn.it, sarac13@gmail.com, isabella.mereu@pg.infn.it, mereuisabella@gmail.com
[9] Dipartimento di Fisica "M. Merlin" dell'Università e del Politecnico di Bari, via Amendola 173, I-70126 Bari, Italy
[10] Istituto Nazionale di Fisica Nucleare, Sezione di Bari, I-70126 Bari, Italy
[11] W. W. Hansen Experimental Physics Laboratory, Kavli Institute for Particle Astrophysics and Cosmology, Department of Physics and SLAC National Accelerator Laboratory, Stanford University, Stanford, CA 94305, USA
[12] Istituto Nazionale di Fisica Nucleare, Sezione di Torino, I-10125 Torino, Italy
[13] Dipartimento di Fisica, Università degli Studi di Torino, I-10125 Torino, Italy
[14] Department of Physics and Astronomy, University of Padova, Vicolo Osservatorio 3, I-35122 Padova, Italy
[15] Laboratoire Leprince-Ringuet, École polytechnique, CNRS/IN2P3, F-91128 Palaiseau, France
[16] Institut für Theoretische Physik and Astrophysik, Universität Würzburg, D-97074 Würzburg, Germany
[17] INAF-Istituto di Astrofisica Spaziale e Fisica Cosmica Milano, via E. Bassini 15, I-20133 Milano, Italy
[18] Italian Space Agency, Via del Politecnico snc, I-00133 Roma, Italy; elisabetta.cavazzuti@asi.it, elisabetta.cavazzuti@ssdc.asi.it
[19] Istituto Nazionale di Fisica Nucleare, Sezione di Roma "Tor Vergata," I-00133 Roma, Italy
[20] Space Science Data Center—Agenzia Spaziale Italiana, Via del Politecnico, snc, I-00133, Roma, Italy
[21] Department of Astronomy, University of Maryland, College Park, MD 20742, USA
[22] INAF Istituto di Radioastronomia, I-40129 Bologna, Italy
[23] Dipartimento di Matematica e Fisica "E. De Giorgi,"Università del Salento, Lecce, Italy
[24] Istituto Nazionale di Fisica Nucleare, Sezione di Lecce, I-73100 Lecce, Italy
[25] Laboratoire d'Annecy-le-Vieux de Physique des Particules, Université de Savoie, CNRS/IN2P3, F-74941 Annecy-le-Vieux, France
[26] Grupo de Altas Energías, Universidad Complutense de Madrid, E-28040 Madrid, Spain
[27] Dipartimento di Fisica "Enrico Fermi,"Università di Pisa, Pisa I-56127, Italy
[28] Catholic University of America, Washington, DC 20064, USA
[29] NASA Goddard Space Flight Center, Greenbelt, MD 20771, USA
[30] Center for Research and Exploration in Space Science and Technology (CRESST) and NASA Goddard Space Flight Center, Greenbelt, MD 20771, USA
[31] Ruhr University Bochum, Faculty of Physics and Astronomy, Astronomical Institute (AIRUB), D-44780 Bochum, Germany
[32] Department of Physical Sciences, Hiroshima University, Higashi-Hiroshima, Hiroshima 739-8526, Japan
[33] Friedrich-Alexander Universität Erlangen-Nürnberg, Erlangen Centre for Astroparticle Physics, Erwin-Rommel-Str. 1, D-91058 Erlangen, Germany
[34] Max-Planck-Institut für Physik, D-80805 München, Germany
[35] The George Washington University, Department of Physics, 725 21st St. NW, Washington, DC 20052, USA
[36] Georg-August University Göttingen, Institute for theoretical Physics—Faculty of Physics, Friedrich-Hund-Platz 1, D-37077 Göttingen, Germany
[37] University of North Florida, Department of Physics, 1 UNF Drive, Jacksonville, FL 32224, USA
[38] Science Institute, University of Iceland, IS-107 Reykjavik, Iceland
[39] Nordita, Royal Institute of Technology and Stockholm University, Roslagstullsbacken 23, SE-106 91 Stockholm, Sweden
[40] Space Science Division, Naval Research Laboratory, Washington, DC 20375-5352, USA
[41] NASA Marshall Space Flight Center, Huntsville, AL 35812, USA
[42] Department of Physics, KTH Royal Institute of Technology, AlbaNova, SE-106 91 Stockholm, Sweden
[43] The Oskar Klein Centre for Cosmoparticle Physics, AlbaNova, SE-106 91 Stockholm, Sweden
[44] School of Education, Health and Social Studies, Natural Science, Dalarna University, SE-791 88 Falun, Sweden

[45] Deutsches Elektronen Synchrotron DESY, D-15738 Zeuthen, Germany
[46] Finnish Centre for Astronomy with ESO (FINCA), University of Turku, FI-21500 Piikiiö, Finland
[47] Istituto Nazionale di Fisica Nucleare, Sezione di Trieste, I-34127 Trieste, Italy
[48] Dipartimento di Fisica, Università di Trieste, I-34127 Trieste, Italy
[49] Institut für Astro- und Teilchenphysik, Leopold-Franzens-Universität Innsbruck, A-6020 Innsbruck, Austria
[50] Department of Physics and Center for Space Sciences and Technology, University of Maryland Baltimore County, Baltimore, MD 21250, USA
[51] Department of Physics, Faculty of Science, Mahidol University, Bangkok 10400, Thailand
[52] Hiroshima Astrophysical Science Center, Hiroshima University, Higashi-Hiroshima, Hiroshima 739-8526, Japan
[53] Department of Physics, Graduate School of Science, University of Tokyo, 7-3-1 Hongo, Bunkyo-ku, Tokyo 113-0033, Japan
[54] Istituto Nazionale di Fisica Nucleare, Sezione di Trieste, and Università di Trieste, I-34127 Trieste, Italy
[55] Università di Udine, I-33100 Udine, Italy
[56] Aryabhatta Research Institute of Observational Sciences (ARIES), Manora Peak, Nainital-263 129, Uttarakhand, India
[57] Osservatorio Astronomico di Trieste, Istituto Nazionale di Astrofisica, I-34143 Trieste, Italy
[58] Center for Space Studies and Activities "G. Colombo,"University of Padova, Via Venezia 15, I-35131 Padova, Italy
[59] Korea Astronomy and Space Science Institute, 776 Daedeokdae-ro, Yuseong-gu, Daejeon 30455, Republic of Korea
[60] Department of Physics, American University, Washington, DC 20016, USA
[61] Centre for Astro-Particle Physics (CAPP) and Department of Physics, University of Johannesburg, P.O. Box 524, Auckland Park 2006, South Africa
[62] Santa Cruz Institute for Particle Physics, Department of Physics and Department of Astronomy and Astrophysics, University of California at Santa Cruz, Santa Cruz, CA 95064, USA
[63] Department of Physics, The University of Hong Kong, Pokfulam Road, Hong Kong, People's Republic of China
[64] Laboratory for Space Research, The University of Hong Kong, Hong Kong, People's Republic of China
[65] Laboratoire Univers et Particules de Montpellier, Université Montpellier, CNRS/IN2P3, F-34095 Montpellier, France
[66] NYCB Real-Time Computing Inc., Lattingtown, NY 11560-1025, USA
[67] Purdue University Northwest, Hammond, IN 46323, USA
[68] Solar-Terrestrial Environment Laboratory, Nagoya University, Nagoya 464-8601, Japan
[69] Department of Physics, University of Maryland, College Park, MD 20742, USA
[70] Institute of Space Sciences (ICE, CSIC), Campus UAB, Carrer de Magrans s/n, E-08193 Barcelona, Spain; and Institut d'Estudis Espacials de Catalunya (IEEC), E-08034 Barcelona, Spain
[71] Institució Catalana de Recerca i Estudis Avançats (ICREA), E-08010 Barcelona, Spain
[72] Praxis Inc., Alexandria, VA 22303, resident at Naval Research Laboratory, Washington, DC 20375, USA
[73] Center for Astrophysics and Cosmology, University of Nova Gorica, Nova Gorica, Slovenia
Received 2021 March 26; revised 2021 May 22; accepted 2021 May 24; published 2021 September 6

Abstract

We present the first Fermi Large Area Telescope (LAT) catalog of long-term γ-ray transient sources (1FLT). This comprises sources that were detected on monthly time intervals during the first decade of Fermi-LAT operations. The monthly timescale allows us to identify transient and variable sources that were not yet reported in other Fermi-LAT catalogs. The monthly data sets were analyzed using a wavelet-based source detection algorithm that provided the candidate new transient sources. The search was limited to the extragalactic regions of the sky to avoid the dominance of the Galactic diffuse emission at low Galactic latitudes. The transient candidates were then analyzed using the standard Fermi-LAT maximum likelihood analysis method. All sources detected with a statistical significance above 4σ in at least one monthly bin were listed in the final catalog. The 1FLT catalog contains 142 transient γ-ray sources that are not included in the 4FGL-DR2 catalog. Many of these sources (102) have been confidently associated with active galactic nuclei (AGNs): 24 are associated with flat-spectrum radio quasars, 1 with a BL Lac object, 70 with blazars of uncertain type, 3 with radio galaxies, 1 with a compact steep-spectrum radio source, 1 with a steep-spectrum radio quasar, and 2 with AGNs of other types. The remaining 40 sources have no candidate counterparts at other wavelengths. The median γ-ray spectral index of the 1FLT-AGN sources is softer than that reported in the latest Fermi-LAT AGN general catalog. This result is consistent with the hypothesis that detection of the softest γ-ray emitters is less efficient when the data are integrated over year-long intervals.

Unified Astronomy Thesaurus concepts: High energy astrophysics (739); Active galactic nuclei (16); Gamma-ray bursts (629); Solar flares (1496); Solar gamma-ray emission (1497); Gamma-rays (637); Gamma-ray sources (633); Catalogs (205); Gamma-ray telescopes (634); Gamma-ray transient sources (1853); Blazars (164); Quasars (1319)

Supporting material: figure set, machine-readable tables, FITS file

1. Introduction

The Large Area Telescope (LAT) on board the Fermi Gamma-ray Space Telescope is an imaging pair-conversion detector operating in the energy range from 20 MeV to >300 GeV. It has a field of view of 2.7 sr at 1 GeV and can provide an image of the entire sky approximately every 3 hr (Atwood et al. 2009). This, together with its large collecting area, makes the LAT well suited to the investigation of γ-ray variable and transient sources. The general (xFGL) catalogs (Abdo et al. 2010f; Nolan et al. 2012; Acero et al. 2015; Abdollahi et al. 2020) were produced by integrating over years of LAT observations. Studies of the counterparts of these LAT cataloged sources are reported in dedicated papers, e.g., the active galactic nucleus (AGN) catalogs named xLAC (Abdo et al. 2010c; Ackermann et al. 2011b, 2015; Ajello et al. 2020). In the Fermi-LAT Third Source Catalog (aka 3FGL, 4 yr of integration; Acero et al. 2015), the last catalog that included monthly light curves for the detected objects, only ∼22% of the sources were found to be variable. The majority of the latter

[74] Funded by contract FIRB-2012-RBFR12PM1F from the Italian Ministry of Education, University and Research (MIUR).

were associated with AGNs, with only a few classes of Galactic sources being found to show variability, i.e., Crab pulsar wind nebula (Tavani et al. 2011), high-mass X-ray binaries (Fermi LAT Collaboration et al. 2009), and galactic novae (Ackermann et al. 2014). In the Fermi-LAT Fourth Source Catalog Data Release 2 (hereafter 4FGL-DR2; Ballet et al. 2020), based on 10 yr of data, the fraction of sources associated with flat-spectrum radio quasars (FSRQs) is less than that associated with BL Lacs. This difference in populations was also found in the previous xFGL catalogs, with the fraction of new sources slightly higher for hard-spectrum sources than for soft-spectrum ones relative to the previous catalog. This could be related to the different variability properties for FSRQs and BL Lacs, as well as to the typically soft γ-ray spectra of FSRQs, while BL Lacs generally show harder spectra (Abdo et al. 2010e). In fact, the sensitivity of the Fermi-LAT[75] improves at a faster rate as a function of exposure for harder sources.[76]

Based on the luminosity function of radio-loud AGNs, however, we would have expected to find more soft γ-ray AGNs whose emission peaks at high frequencies in the inverse Compton regime (Ackermann et al. 2011a) than those that were detected in the xFGL catalogs (Abdo et al. 2010c; Ackermann et al. 2011b, 2015).

Following these premises, soft-spectrum objects that have low duty cycle would not be detectable in the years-long integration of xFGL catalogs but could be detectable during brief periods of enhanced γ-ray activity. Searches for variable sources have already been carried out for this reason by the Fermi-LAT collaboration using different techniques. The Monitored Source List[77] provides daily and weekly light curves of the brightest sources and transients found during LAT observations. Variability on timescales of 6 hr and 1 day is monitored by the Fermi Flare Advocate program (Ciprini & Fermi-LAT Collaboration 2012) using the quick-look science data products of the Automated Science Processing pipeline (Chiang 2012). Finally, the Fermi All-sky Variability Analysis (Ackermann et al. 2013 and Abdollahi et al. 2017) uses a photometric technique to blindly search the data for transients over the entire sky on weekly time intervals. The latter analysis is independent of any model for the diffuse and isotropic γ-ray emission, and it produced a list of 215 and 518 flaring γ-ray sources (including those already listed in the xFGL catalogs) over 3.9 and 7.4 yr of integration, respectively.

In this work we present the First Fermi Gamma-ray LAT Transient Catalog (1FLT), a census of sources located at $|b| > 10^\circ$ and detected by scanning a decade of Fermi-LAT data over monthly time intervals. In Section 2 we describe the analysis procedure used to search for new source candidates and the maximum likelihood (ML) analysis used to estimate their significance. In Section 3 we describe the methods used to perform a positional association of the new sources with those listed in several radio, infrared, optical, and X-ray catalogs. In Section 4 we discuss the spectral properties of the 1FLT catalog and the results of the comparison with the sources reported in the fourth Fermi-LAT catalog of AGNs (4LAC; Ajello et al. 2020) in order to investigate the differences between the γ-ray sources detected in short and long integration times. In Section 5 we discuss the comparison with the second catalog of flaring γ-ray sources (2FAV; Abdollahi et al. 2017) and describe some particular sources. Finally, in Section 6 we report our results and conclusions of this new strategy for the detection of variable γ-ray sources.

[75] https://www.slac.stanford.edu/exp/glast/groups/canda/lat_Performance.htm

[76] This is because the LAT point-spread function (PSF) at low energies is broader, and therefore the soft-spectrum sources reach the confusion limit. On the other hand, at higher energies the PSF is relatively narrow. Hard-spectrum sources emit many more high-energy photons than soft sources, leading to more precise localizations and, in turn, more reliable associations.

[77] https://fermi.gsfc.nasa.gov/ssc/data/access/lat/msl_lc/

2. Fermi-LAT Data Analysis

The data used in this work encompass a 10 yr period from 2008 August 4 15:43:36 UTC (Mission Elapsed Time (MET) 239557417) to 2018 August 5 10:23:32 UTC (MET 555157417). They are analyzed in monthly time bins, where one time bin (TBIN) is defined as 2,630,000 s (~30 days). The 1FLT is constructed in the energy range from 100 MeV to 300 GeV using the `Pass8` SOURCE class events, in combination with `P8R3_SOURCE_V2` instrument response functions (IRFs; see footnote 75). The exposure of the Fermi-LAT is fairly uniform across the sky, but the brightness of the interstellar diffuse γ-ray background, and hence the sensitivity for source detection, depends strongly on the Galactic latitude. For this reason we apply a further cut, considering only data with Galactic latitude $|b| > 10^\circ$.

We applied a zenith angle cut of $<90^\circ$ in order to reduce the contamination from the Earth limb and the standard data quality cuts (DATA_QUAL > 0 && LAT_CONFIG $== 1$) for the extraction of good time intervals. We selected only "SOURCE" event class (LAT EVENT_CLASS $= 128$) and event type "FRONT+BACK" (LAT EVENT_TYPE $= 3$). We repeated the monthly binned analysis selecting data with a 15-day shift, that is, with the first 1-month time bin starting on 2008 August 19 13:39:59 UTC (MET 240846000). This improves the sensitivity for sources that may display variable activity at the edges of the time bins. Adopting this procedure, we have analyzed a total of two sets of 120 monthly data sets, which are not independent since they partially overlap. In the following we refer to these two sets as follows: "nominal" for the first set starting on 2008 August 4, and "shifted" for the second set starting on 2008 August 19.

2.1. Source Detection and Localization

We have partitioned each of the 240 monthly TBINs into 192 circular regions of interest (ROIs) centered on points defined by means of a HEALPix[78] sky pixelization (Górski et al. 2005) with $N_{\rm side} = 4$ and adopting celestial coordinates. The ROIs include events in cones of 15° radius about the center of the pixel. The ROIs constructed in this way are not independent, as they partially overlap.

To identify the candidate sources (seeds), we used a wavelet transform analysis (Damiani et al. 1997) using the *PGWave* tool (Ciprini et al. 2007). *PGWave* works on the square images inscribed in ROIs of 15° radius; therefore, the side of the square images is $15^\circ\sqrt{2} \sim 21.2$ degrees. We adopted a pixel size of $0^\circ.25$ and the stereoscopic projection for the images. We performed the analysis independently on each ROI and TBIN deleting the seeds located at the border of the ROI (distance from the ROI center $>10^\circ$) in order to avoid edge effects. In this way we obtained 129,802 seeds in the nominal months and 133,673 seeds in the shifted ones.

[78] http://healpix.sourceforge.net

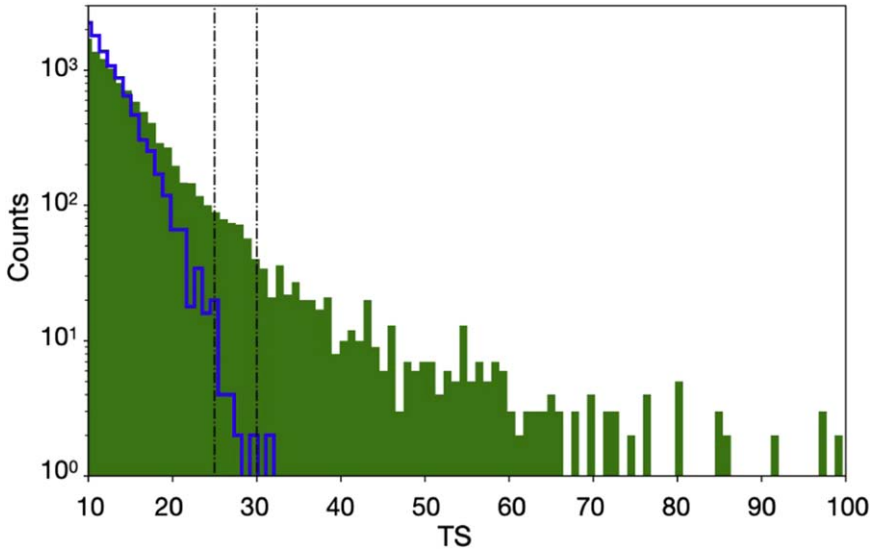

Figure 1. Distributions of TS evaluated for the simulated skies (blue curve) and the actual skies (shaded green). The results obtained in the simulation on 120 months are represented multiplied by two to account also for the shifted months. The two vertical lines show the TS range of low-confidence sources ($25 < \mathrm{TS} < 30$).

After the seed extraction, we performed an ML analysis on all seeds that had Galactic latitude $|b| > 10°$ and that had an angular distance greater than 50′ from any 4FGL-DR2 source (with this selection we excluded ∼10% of the extragalactic sky). The conservative 50′ cross-correlation radius corresponds to the average plus 1σ value of the distribution of the 1FLT catalog's semimajor axis of the error ellipses at 95% confidence level (Conf_95_SemiMajor in Table A1). The ML analysis provides the evaluation of the test statistic (TS), defined as $\mathrm{TS} = 2\Delta\log\ \mathcal{L}$ (Mattox et al. 1996), which quantifies how significantly a source emerges from the background comparing the likelihood function $\mathcal{L}$ with and without a source. We performed the final localization only for seeds with $\mathrm{TS} > 10$ (4872 for the nominal months and 4737 for the shifted ones).

We evaluated the significance of the detection and the spectral parameters for the newly found sources by performing a binned ML with eight bins per decade in energy and 0.°1 binning in Galactic coordinates. For each point source we assumed a power-law spectrum defined as $dN/dE = K*(E/E_0)^{-\Gamma}$, where K is the flux scale factor, Γ is the spectral index, and E_0 is the reference energy ($E_0 = 1$ GeV). The ROI model used in the likelihood analysis contained all *PGWave* seeds found (including also the ones associated with 4FGL-DR2 sources) in the selected month in an ROI of $10° \times 10°$ square, centered at the position of the target, along with the Galactic and isotropic diffuse backgrounds.[79] To perform the analysis, we used the *Fermitools* 1.2.1 package available from the Fermi Science Support Center (FSSC)[80] and the *Fermipy* 0.18.0 software package (Wood et al. 2017). We use $\mathrm{TS} = 25$ as the detection threshold, corresponding to a significance of $\sim 4\sigma$ assuming a χ^2 distribution with 4 degrees of freedom (position and spectral parameters of a power-law source; see Mattox et al. 1996).

2.2. False-positive Estimation and Source Detection Efficiency

The evaluations of the false-positive rate and efficiency are fundamental to assess the reliability of the adopted method in the detection of transient sources. In order to calculate the false-positive, rate we simulated 120-month-long data sets, including in the model only the Galactic and the extragalactic diffuse emissions. Over month-long timescales the false positives are dominated by statistical fluctuations of the background rather than systematic effects. For the simulations we adopted the analysis of the 1FLT. We identified the seeds as described in Section 2.1 and performed the binned ML analysis assuming a power-law spectrum for each seed. The distributions of the statistical significance of the candidate sources found in the fake and true skies are shown in Figure 1. In the 120 simulated skies we found 12 spurious detections with $\mathrm{TS} > 25$ over ∼24,000 seeds, and one and two detections with $\mathrm{TS} > 30$ and $\mathrm{TS} > 28$, respectively. To be conservative, in the estimation of the spurious detections in the real data these numbers should be multiplied by a factor of two to account also for the shifted months. Therefore, we may expect 24 fake detections with $\mathrm{TS} > 25$.

Since our adopted threshold of $\mathrm{TS} > 25$ still includes a nonnegligible number of spurious sources, in the 1FLT catalog $\mathrm{TS} > 25$ candidate sources are flagged as low-confidence when they are detected in only one TBIN and have a TS value between 25 and 30. A total of 72 1FLT sources are flagged as low-confidence. Each individual low-confidence source has a probability of about 34% of being spurious.

To assess the detection efficiency we used astrophysical γ-ray sources known to be steady in flux such as pulsars (PSRs) located at high latitude reported in the 4FGL catalog. The majority of sources taken in consideration for the estimation of efficiency are millisecond pulsars.

For each TBIN of data we applied the analysis procedures targeting the selected PSRs, and we compared the number of detections obtained as a function of energy flux to the total number of pulsars (efficiency of 100% when we had a significant detection of the PSRs in all 240 months). Figure 2 represents the rate of detection over 240 months for the selected PSRs as a function of energy flux. As suggested in Principe et al. (2018), we modeled the detection efficiency with a hyperbolic tangent function $\tanh\lambda(f - f_0)$, where the two parameters λ and f_0 are determined by fitting to the detection

[79] https://fermi.gsfc.nasa.gov/ssc/data/access/lat/BackgroundModels.html
[80] https://fermi.gsfc.nasa.gov/ssc/data/analysis/

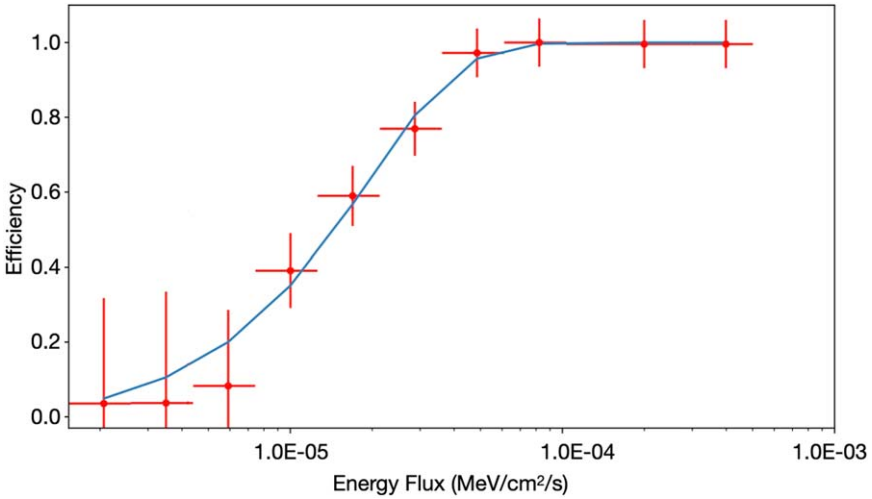

Figure 2. Detection rate as a function of the energy flux of high-latitude PSRs. Each point represents the ratio of detected sources over 240 overlapping months with respect to the number of true 4FGL PSRs with $|b| > 10$ binned by flux. The error bars correspond to the statistical uncertainty estimated using the binomial statistic. The blue curve is the hyperbolic tangent function $\tanh\lambda(f - f_0)$.

efficiency points. We obtained the following values: $\lambda = 4.0 \times 10^4\,\mathrm{MeV}^{-1}\,\mathrm{cm}^2$ s and $f_0 = 8.41 \times 10^{-7}$ MeV cm^{-2} s^{-1} with a χ^2 of 0.93 with 9 degrees of freedom.

2.3. The 1FLT Catalog Construction

The 1FLT catalog lists all the sources that satisfy the following criteria: a TS > 25, a ratio between the flux error and the flux $\Delta\mathrm{Flux}/\mathrm{Flux} < 0.5$, and a power-law index $\Gamma < 4.5$. We associated multiple detections with the same source when they are spatially coincident with 2D-sky cross-correlation using the error ellipses at 95% confidence level. We manually checked each individual multiple association to verify the automatic procedure, and in three cases we did not consider the sources as multiple detections since the centroids of the γ-ray emission were visually not cospatial (1FLT J0240−4657 and 1FLT J0240−4739; 1FLT J0519−3709 and 1FLT J0527−3747; 1FLT J1322−4521 and 1FLT J1323−4439). When the same source was detected on different but overlapping ROIs, we reported the results of the most significant detection. A reference of this repeated occurrence is reported in the catalog column "repROI." For instance, see Appendices A and B, as well as the catalog file.

The final 1FLT catalog is composed of 142 unique transient sources not associated with any 4FGL-DR2 emitters: 64 sources detected in the nominal 120 months and 78 in the shifted 120 months. Seventy-two 1FLT sources with $25 <$ TS < 30 are flagged as low-confidence (as reported in Section 2.2). The complete list of sources is available in electronic format (FITS format) as supplementary material. The columns are described in Appendix A in Tables A1–A3. In Appendix B, Table B1 has the 1FLT list. The source designation is 1FLT JHHMM+DDMM.

Out of these 142 1FLT sources, 108 1FLT sources were detected only once, i.e., in one single TBIN, while 34 other distinct 1FLT sources displayed significant gamma-ray emission in more than one TBIN. These 34 sources listed in 1FLT correspond to their most significant detection in each relative cluster of multiple flaring episodes. Forty-four remaining flaring episodes are listed in the extension `FLARES` of the electronic release that includes other useful information specific to each flaring episode, such as time, localization, flux, significance, and spectral parameters. The column "Flares" in Table B1 contains the number of flaring episodes of each 1FLT source. In case of multiple detections of positionally consistent candidates, the source name is based on the position of the candidate detection with the largest value of TS.

The 1FLT method allowed us to collect also 60 detections associated with the Sun and 27 associated with 14 of the brightest Fermi-LAT γ-ray bursts (GRBs). In Appendix B, Table B2 lists the Sun detections, and Table B3 contains GRB detections.

The sky locations of the 1FLT sources, together with Sun and GRB detections, are shown in Figure 3.

To evaluate the possible contamination by the Moon of the 1FLT source catalog, we checked the times and trajectories of the passage of the Moon through the 1FLT fields. For the overlaps between the Moon's path and 1FLT source localization we extracted the 1FLT fluxes with a 1-day timescale in the referring month, to verify simultaneously the coincidence in time and space. We found no evidence for the Moon being confused with any 1FGL detection because when we detected the higher 1-day time bin flux the Moon localization was more than 5° away from the 1FLT-derived position.

2.4. Gamma-Ray Spectra and Light Curves

For each source in the 1FLT catalog we extracted the γ-ray spectrum and monthly binned light curve. The spectral energy distributions (SEDs) are produced in three energy bands (i.e., 0.1–1 GeV, 1–10 GeV, 10–100 GeV)[81] by modeling the 1FLT source with a power-law spectrum with free normalization and a spectral index fixed to 2. When the TS of the spectral bin was less than 4 or the value of spectral data point error was greater than 50% of the measured value, we calculated the upper limit at 2σ confidence, using the Bayesian computation if TS < 1 (Helene 1984). The γ-ray spectral data points (νF_ν) are reported in the catalog available in electronic format as supplementary material.

The light curves were produced using the binned ML technique, over the energy range of 100 MeV–300 GeV. The

[81] We did not report in the catalog the last energy band (100–300 GeV) since it does not give any further information.

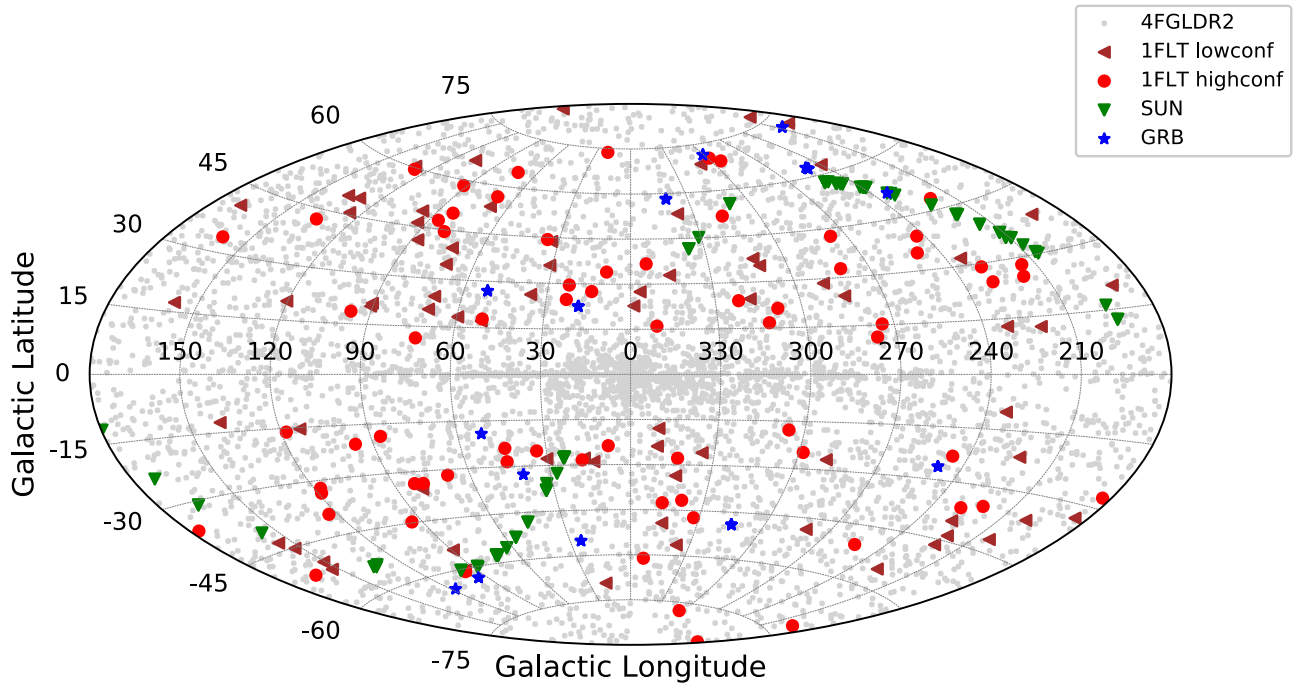

Figure 3. Aitoff projection of 1FLT sources represented in Galactic coordinates (high-confidence sources: red filled circles; low-confidence sources: brown filled triangles), Sun detections (green filled triangles), and GRB detections (blue filled stars) superimposed on 4FGL-DR2 sources represented in gray.

likelihood fit followed the same procedure described above (see Section 2), fixing the photon index of the 1FLT source to the 1FLT catalog value. The ROI model included all *PGWave* seed detections of the TBIN located in an ROI of 10° centered at the 1FLT catalog position of the source of interest. When the target was detected with TS < 4, or the number of its predicted photons was $N_{\rm pred} < 3$, or the uncertainty on its flux estimate was large ($\Delta{\rm Flux}/{\rm Flux} > 0.5$), upper limits were calculated based on the method of Helene (1984). For consistency with the 1FLT catalog procedure, the light curves start coherently with the nominal or shifted time selection. The statistical uncertainty on the fluxes is typically larger than the systematic uncertainty (Ackermann et al. 2012), and only the former is considered in this paper. All light curves are shown in Appendix C.

3. Source Association

To identify candidate counterparts of the 142 γ-ray sources reported in the 1FLT, we used two approaches: the Bayesian method, extensively described in the xFGL catalogs (see, e.g., Acero et al. 2015; Abdollahi et al. 2020), and the positional method, which relies solely on the location of the counterpart inside the error ellipse. To estimate the probability that a specific counterpart association is likely to be real, the Bayesian approach trades the positional coincidence of possible counterparts with 1FLT sources against the expected number of chance coincidences. Similarly to what was done in the xFGL catalogs, in the 1FLT we retained associations if they had a posterior probability of at least 80%. For the source association analysis we first checked the same catalogs used to build the 4FGL (see Abdollahi et al. 2020). We performed the Bayesian association procedure on each of the 240 skies for all the candidate seeds with a localization evaluation, each month (i.e., TBIN) being an independent sky (see Section 2 for sky/TBIN correspondence definition).

For 1FLT sources without a Bayesian association, we searched the 95% confidence error ellipse for the presence of promising, not yet known, γ-ray-emitting sources. This search was carried out using the *SSDC Tools*[82] and *VOU-Blazar Tool*[83] (Chang et al. 2020). In particular, the *VOU-Blazar Tool* allowed us to retrieve all possible blazar candidates within a specified area of the sky. The complete list of catalogs used by the *VOU-Blazar Tool* can be found in Brandt (2018). This method enables the association of the sources with radio surveys that are not used by the Bayesian association method. For 1FLT sources with large positional error ellipses more than one candidate counterpart was found. In these cases, as well as when no candidate counterparts were found, we flagged the 1FLT source as unassociated.

3.1. Class Designation

In order to classify candidate γ-ray counterparts, we used either the optical classifications published in the BZCAT list (a compilation of sources classified as blazars; Massaro et al. 2015) or the spectra available in the literature or from online databases. The main ones are the Sloan Digital Sky Survey (SDSS; Alam et al. 2015; Albareti et al. 2017; Abolfathi et al. 2018) and the 6dF Galaxy Survey (Jones et al. 2009). The classes have been assigned with the following criteria:

1. FSRQ, BL Lac-type object, compact steep-spectrum radio source (CSS), steep-spectrum radio quasar (SSRQ), and radio galaxy (RG): sources with a well-established classification in the literature and/or through a good-quality optical spectrum;
2. blazar candidate of uncertain type (BCU): an object in the listed BZCAT as blazar of uncertain/transitional type or a source with blazar multiwavelength characteristic—flat radio spectrum and double-humped, broadband SED;

[82] https://tools.ssdc.asi.it/
[83] http://www.openuniverse.asi.it/

Table 1
Census of 1FLT Sources

Class	Class Description	Number
FSRQ	Flat-spectrum radio quasar	24
BLL	BL Lacertae object	1
CSS	Compact steep-spectrum radio source	1
SSRQ	Steep-spectrum radio quasar	1
RG	Radio galaxy	3
BCU	Blazars of uncertain type	70
AGN	Active galactic nuclei of other type	2
UNASS	Unassociated	40

3. nonblazar active galaxy: for these candidate counterparts the existing data do not allow an unambiguous determination of the AGN type;
4. unassociated: sources without an unequivocal counterpart or without any plausible candidate at other wavelengths

The class designations for the 1FLT sources are listed in Table 1.

3.2. Census

As reported in Table 1, the 1FLT includes 142 sources, with 24 FSRQs, 1 BL Lac, 1 CSS, 1 SSRQ, 3 RGs, 70 BCUs, and 2 other AGNs. This sample is composed exclusively of jetted AGNs, which is also the largest population present in the xFGL catalogs. The sample composition, however, is different when compared to that of the Fermi-LAT general catalogs. There are 24 FSRQs, which represents a higher fraction as compared to the xFGL catalogs. Twenty-seven sources are associated with the Bayesian method, 75 with the positional method. Forty sources remain unassociated (28.2%). This fraction is similar to that reported in the xFGL catalogs. The low-confidence sample includes 72 sources, among which associations are found with 29 BCUs, 1 BL Lac, 10 FSRQs, 2 RGs, 1 SSRQ, and 2 other types of AGNs. These low-confidence sources were associated with the Bayesian method in four cases (one BCU and three FSRQs). The high-confidence sample includes 70 sources, among which associations are found with 41 BCUs, 1 CSS, 14 FSRQs, and 1 RG. In this sample, the Bayesian method finds 23 associations (1 CSS, 5 FSRQs, and 17 BCUs). 1FLT includes six sources that are associated with a source from previous FGL catalogs (1FGL, 2FGL, 3FGL) but that do not have a counterpart in the 4FGL-DR2 list. These associations are reported in the catalog table in the column named *ASSOC_FERMI*. In that column we also include the associations (14 1FLT sources) with the preliminary 8 yr Fermi-LAT source list (FL8Y).[84] In the catalog table column *ASSOC_GAM* we report the associations with other γ-ray source lists: one association in the Second AGILE catalog of gamma-ray sources (Bulgarelli et al. 2019), two associations in the Swift-BAT 105-Month Hard X-ray Survey (Oh et al. 2018), and one association in the INTEGRAL/IBIS AGN catalog (Malizia et al. 2016).

4. Properties of 1FLT Sources

4.1. Spectral Properties

Figure 4 shows the distribution of the power-law photon index Γ for the 1FLT sources, along with that for the 4LAC sources that are associated with FSRQs and BL Lacs. The 1FLT distribution extends to softer Γ values (median value of $\Gamma \sim 2.7$) than those of the 4LAC sources (median value of $\Gamma \sim 2.2$ or 2.5 if we consider only 4LAC FSRQs). As shown in Figure 4, 26 1FLT sources exhibit softer spectral indices than the softest 4LAC FSRQ. We performed the Kolmogorov–Smirnov (K-S) test (Kolmogorov 1933) to evaluate whether the 1FLT spectral index distribution comes from the same parent population of 4LAC subclass distributions (null hypothesis). We found that our null hypothesis is rejected in all cases at a confidence level of 99.9% ($\alpha = 0.001$). The identification of these soft-spectrum sources shows that integrating over monthly timescales allowed us to investigate the soft part of the gamma-ray source distribution, which is usually suppressed (or confused with the low-energy component of the γ-ray background) when analyzed over longer, multiyear timescales.

The population of soft-spectrum gamma-ray sources could include members of the so-called "MeV-blazars" (blazars that are exceptionally bright at MeV energies; Bloemen et al. 1995; Blom et al. 1995). These objects have shown variability in their γ-ray flux when integrated over timescales of months. However, their variability timescales are longer than those shown by harder-spectrum blazars (Sikora et al. 2002). The MeV-peaked emission can be modeled with the external Comptonization of accretion disk radiation or of the near-IR emission of hot dust (Bednarek et al. 1996). The transient nature of the MeV-blazar phenomenon is evidence for the presence of this population of soft FSRQs with a steep Γ ($E > 100$ MeV) on an approximately 1-month timescale. The month-scale variability and the pronounced increase of the emission in the keV–MeV regime are also reported by Kreter et al. (2020) in their search for high-redshift blazars. The large distances of these sources and the subsequent redshifting of their emission mean that the γ-ray emission is shifted toward longer wavelengths.

4.2. Spectral Energy Distribution Classification

For all of the 1FLT sources associated with blazars we collected the available multifrequency data in order to infer the synchrotron peak frequency ν^{S}_{peak} of the observed broadband SED, which was in turn used to perform an SED-based classification. We classified blazars as low synchrotron peaked (LSP, $\nu^{S}_{peak} < 10^{14}$ Hz), intermediate synchrotron peaked (ISP, 10^{14} Hz $< \nu^{S}_{peak} < 10^{15}$ Hz), or high synchrotron peaked (HSP, $\nu^{S}_{peak} > 10^{15}$ Hz). In this procedure we used a compilation of broadband archival data as described for the 2LAC (Ackermann et al. 2011b). The estimation of ν^{S}_{peak} relies on a third-degree polynomial fit of the low-energy hump of the SED that is performed on a source-by-source basis (the procedure was adopted in Ackermann et al. 2015). With this procedure we reconstructed the ν^{S}_{peak} for only 65 1FLT sources owing to the limited multifrequency sampling. Figure 5 shows the power-law index versus the ν^{S}_{peak} for both the 1FLT and 4LAC sources. The strong correlation evident in the 4LAC sample appears to be diluted for the sources in the 1FLT catalog since we detected only LSP sources with soft spectra. We noted, however, that the number of 1FLT catalog sources with ν^{S}_{peak} estimation is just a few percent of those in the 4LAC catalog.

[84] https://fermi.gsfc.nasa.gov/ssc/data/access/lat/fl8y/

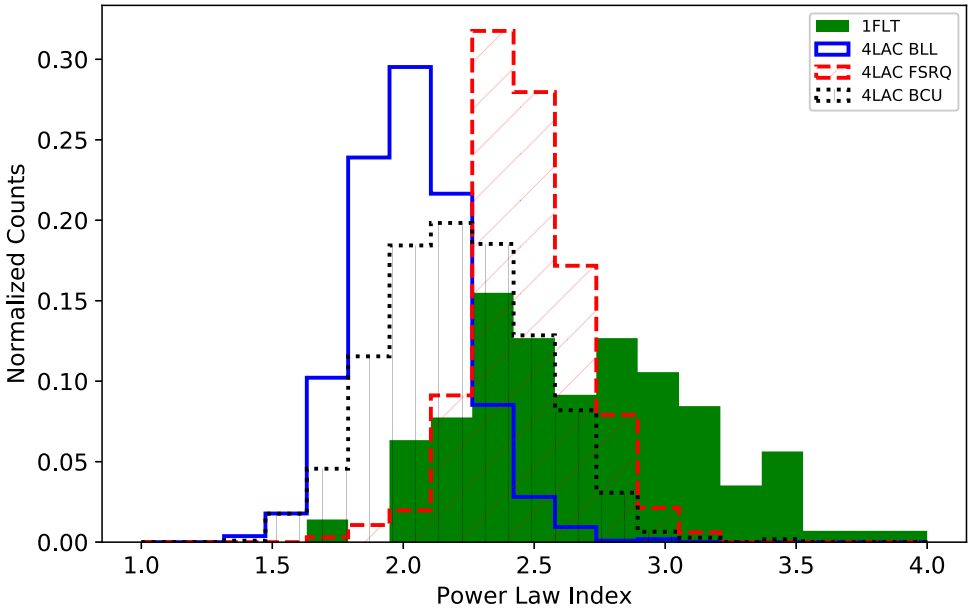

Figure 4. Normalized distribution of power-law index for 1FLT sources (green filled histogram) and 4LAC sources. The blue line represents the 4LAC BL Lac objects, the red dashed line 4LAC FSRQ objects, and the black dotted line 4LAC BCU objects.

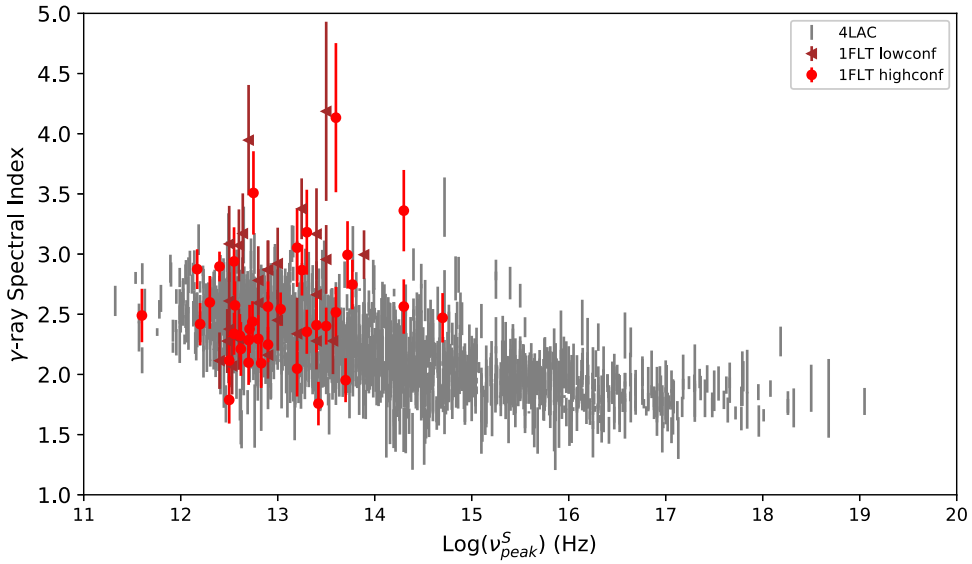

Figure 5. Power-law index of 1FLT sources plotted as a function of SED $\nu^S_{\rm peak}$ (high-confidence sources: red filled circles; low-confidence sources: brown filled triangles); 4LAC data points are shown in gray for comparison.

4.3. Luminosity, Radio Flux, and Redshift

For each 1FLT source that has a counterpart with a known redshift, we computed the γ-ray and radio luminosity using the ΛCDM cosmological parameters obtained by Planck (Planck Collaboration et al. 2014); in particular, we used $h = 0.67$, $\Omega_m = 0.32$, and $\Omega_\Lambda = 0.68$, where the Hubble constant $H_0 = 100h\,{\rm km\,s^{-1}\,Mpc^{-1}}$. Redshifts are available for a total of 30 1FLT sources: all FSRQs, 1 BCU, 1 BLL, 3 RG, and 1 nonblazar object.

Analyzing the distribution of spectral index versus γ-ray luminosity for all the sources of our sample, along with the corresponding values for all sources of the 4LAC (Ajello et al. 2020), plotted in Figure 6, we can see that the 1FLT sources and the 4LAC sources occupy different regions of the parameter space. The 1FLT sources show greater γ-ray luminosities, possibly because they are detected during flaring states, and softer γ-ray spectra than the sources detected by integrating over years-long periods. When integrating over short time intervals, sporadic flaring activity is detected from a subluminous population whose integrated emission would not have been detected over longer time intervals, due to their weak quiescent flux being merged into the integrated background gamma-ray emission. It is noteworthy that more than half of the 1FLT sources lie in a region of the parameter space that is only sparsely populated by 4LAC sources.

Plotting the ratio of γ-ray luminosity to radio luminosity as a function of $\nu^S_{\rm peak}$ (Figure 7), we can see that the ratio is clearly greater for the 1FLT than for the 4LAC; this could be explained simply by the fact that the γ-ray flux detection and the radio flux measurement are not simultaneous and the gamma-ray measurements are by definition made during γ-ray flaring episodes. These sources are in fact very bright during a flare but

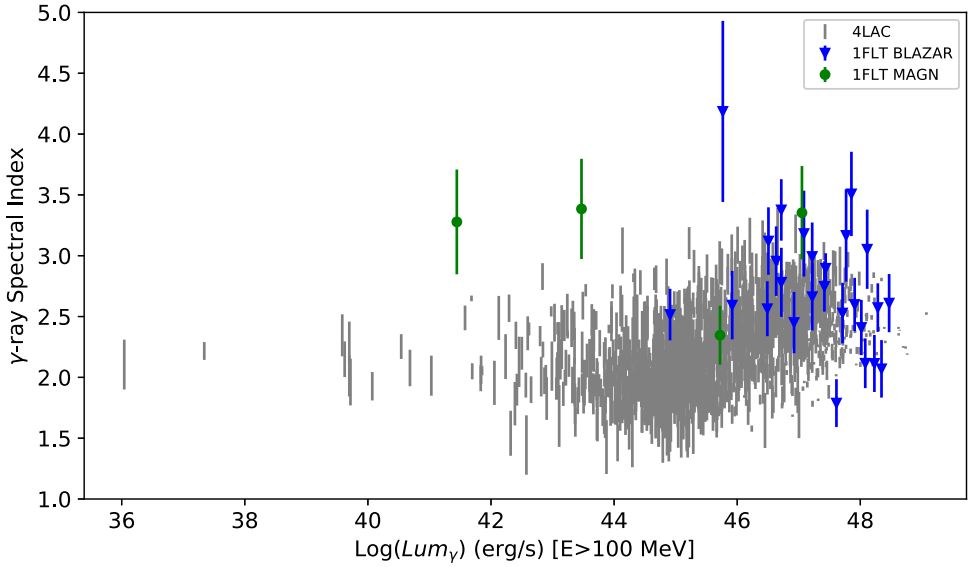

(a)

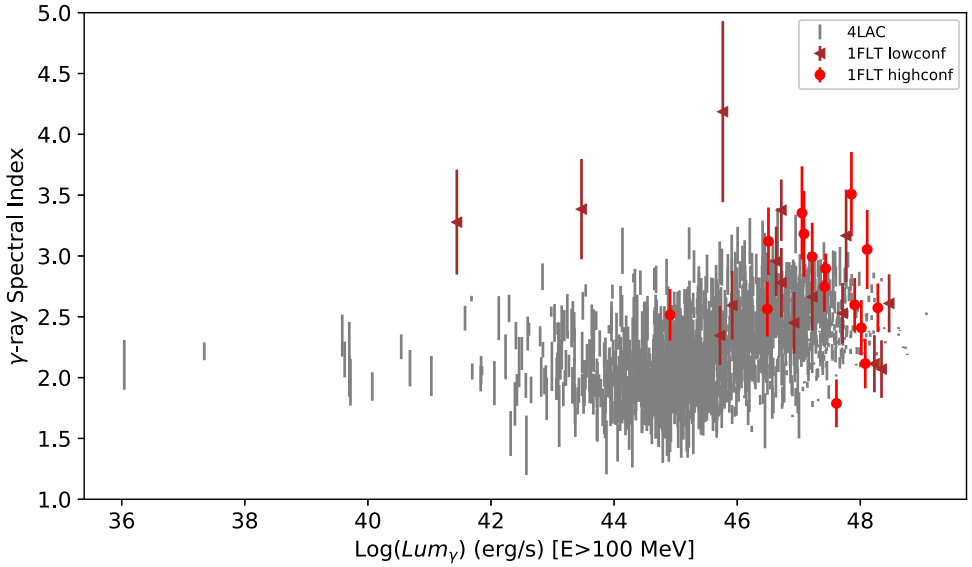

(b)

Figure 6. Power-law index of all 1FLT sources, plotted as a function of the γ-ray luminosity (100 MeV–300 GeV). (a) Green filled circles represent 1FLT misaligned AGN (MAGN); blue filled triangles represent 1FLT blazars. (b) Red filled circles represent 1FLT high-confidence sources; brown filled triangles represent 1FLT low-confidence sources. 4LAC data points are shown in gray for comparison.

show a faint long-term integrated γ-ray flux, which limits their possibility of being detected significantly on the long-term periods typically considered for xFGL catalogs.

In terms of the distribution of the radio fluxes for the 1FLT sources, our sources show fainter fluxes than those of the 4LAC FSRQs (using a K-S test, we found that our null hypothesis is rejected at a confidence level of 99.9%) but are comparable to those of the 4LAC BCUs as shown in Figure 8 (using a K-S test, we found that the two data sets are not very similar but do not differ by enough that we could reject the null hypothesis: $p = 2.14\%$ and distance $= 0.16$). This is because most of the 1FLT sources are BCUs.

Figure 9 shows the redshift distributions for 4LAC FSRQs and 1FLT sources. The redshift is available for all FSRQs, 1 BCU, 1 BLL, 3 RG and 1 nonblazar object. The 1FLT redshift distribution shows a peak at low redshift (<1). This peak is due to the contribution of 1FLT misaligned AGNs. These sources show a larger jet inclination angle, where de-boosted radiation makes the relativistic jet radiation weaker and more difficult to detect in γ-rays (Abdo et al. 2010d). However, $\sim$50% of FSRQs are detected at $z > 1$, suggesting a different distribution. Another effect, in fact, that can be seen in Figure 9 is that there is an additional peak at $z > 2$, unlike the 4LAC distribution, which includes only a small fraction of objects at $z > 2$. This shows that the 1FLT method is well suited for detecting high-redshift blazars. These results are in agreement with the behavior of the population of high-redshift blazars reported in Kreter et al. (2020).

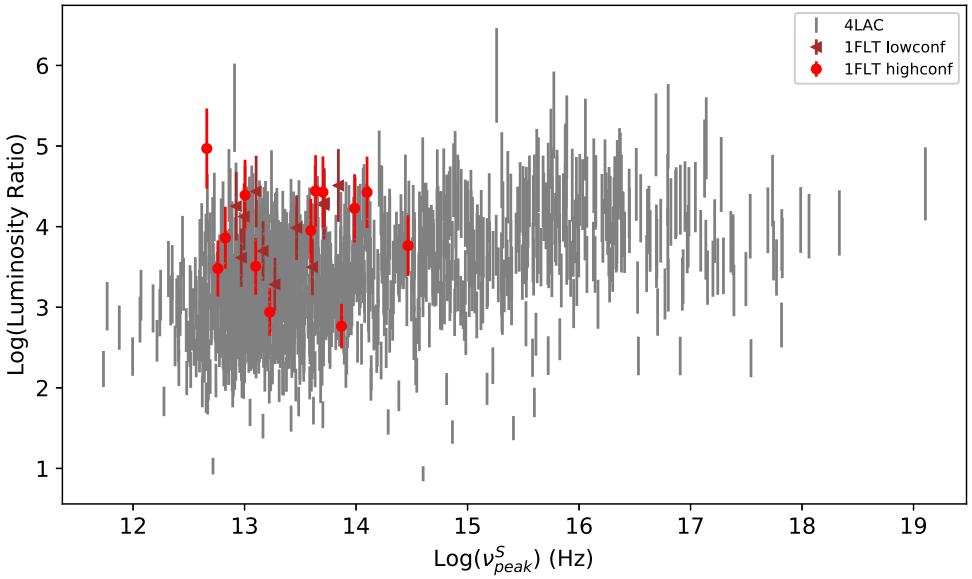

Figure 7. Ratio of γ-ray to radio luminosity plotted as a function of SED $\nu^S_{\rm peak}$. Red filled circles represent 1FLT high-confidence sources; brown filled triangles represent 1FLT low-confidence sources. 4LAC data points are shown in gray for comparison.

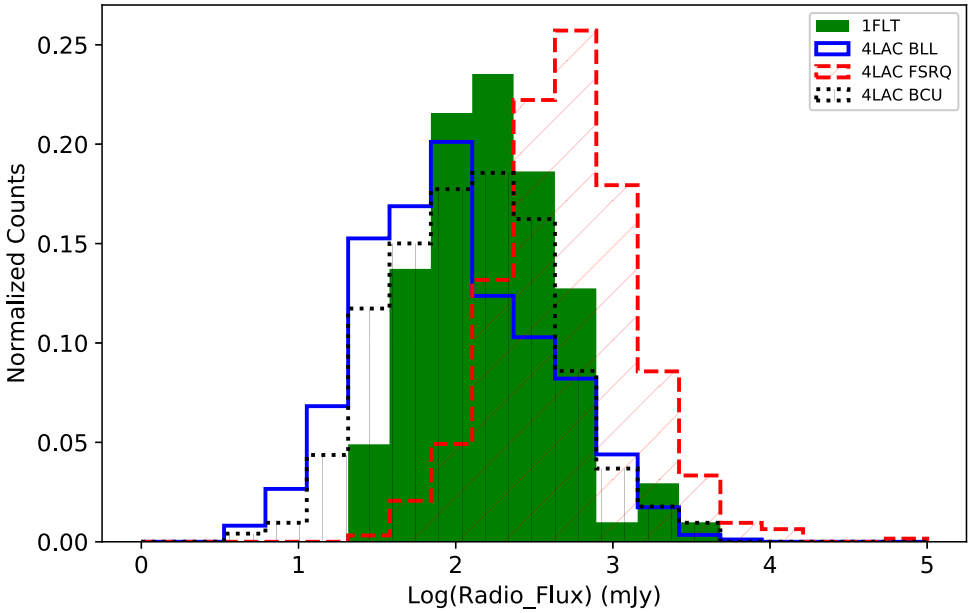

Figure 8. Histograms of radio flux density at 1.4 GHz for the 1FLT sources (green) and 4LAC sources. The blue solid line represents 4LAC BL Lac objects, the red dashed line 4LAC FSRQs, and the black dotted line 4LAC BCU objects.

5. Discussion

5.1. Comparison with the Second FAVA Catalog

The Fermi All-sky Variability Analysis (FAVA) searches for transient sources over the entire sky observed by the Fermi-LAT on 1-week time intervals. The second catalog of flaring γ-ray sources (2FAV) spans the first 7.4 yr of Fermi-LAT observations and reports 518 variable γ-ray sources with significances of at least 6σ. Based on positional coincidence, candidate counterparts have been found for 441 sources, most of them blazars. The catalog also provides for each source the time, location, and spectrum of each flaring episode (Abdollahi et al. 2017).

Given the variable nature of 2FAV sources, we decided to compare the 1FLT catalog to the 2FAV catalog. We have investigated positional (within the error ellipses) and time correspondence between 1FLT sources and 2FAV sources.

We found correspondence in position and time for a few sources: 1FLT J1732+1510 (TBIN 71.5) with 2FAV J1732 +15.2 (reported in an Astronomer's Telegram,[85] ATel#6395), 1FLT J1919−4543 (TBIN 21) with 2FAV J1919−45.7 (ATel#2666), 1FLT J1936+5341 (TBIN 20.5) with 2FAV J1936+53.7, and 1FLT J2010−2523 (TBIN 72.5) with 2FAV J2009−25.4 (ATel#6553). The associations with 2FAV catalog sources are reported in the column named *ASSOC_FAVA* in the 1FLT catalog table. These 2FAV sources have the same counterparts as the corresponding 1FLT sources except in

[85] http://www.astronomerstelegram.org

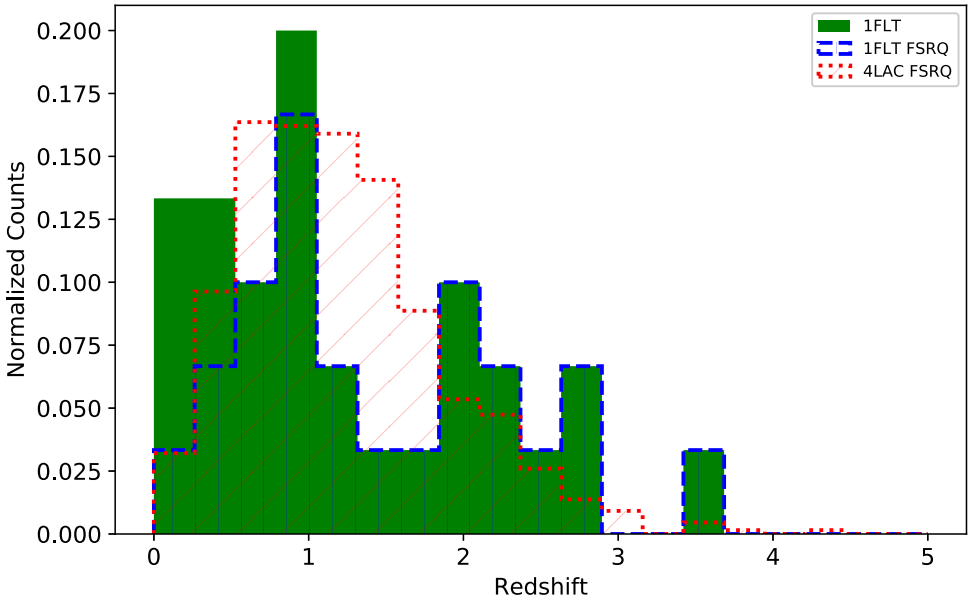

Figure 9. Redshift distributions for 1FLT (green shaded region), 1FLT FSRQ (blue dashed line), and 4LAC FSRQ (red dotted line) sources.

the case of 2FAV J1936+53.7, which is not associated, and 1FLT J1936+5341, which we associated with TXS 1935+536.

Looking at γ-ray candidate seeds in the 1FLT search with TS < 25 and not already in 4FGL-DR2, we found correspondence in position and time with two other 2FAV sources. 2FAV J0539−28.8 corresponds to a detection in TBIN 55 with TS $= 9$ and 2FAV J2056−11.5 to a detection in TBIN 60.5 with TS $= 14$. We attribute this to the dilution over the month timescale of the γ-ray emission that occurred during a brief (about 1 week) flare. This result confirms the potential of Fermi to find new sources when the data are integrated over different time intervals. It also shows that choosing a monthly time interval allows us to detect a different and new population of sources than those found when the data are binned on weekly timescales.

5.2. Duty Cycle Evaluation

The duty cycle for an astronomical object of a given class was defined by Romero et al. (1999) as

$$\mathrm{DC} = 100\frac{\sum_{i=0}^{n} N_i 1/(\Delta t_i)}{\sum_{i=0}^{n} 1/(\Delta t_i)}\%, \quad (1)$$

where $\Delta t_i = \Delta t_{i,\mathrm{obs}}(1+z)^{-1}$ is the duration (corrected for redshift z) of a monitoring interval of a source of the selected class and N_i is equal to 0 when the source is not variable at $\Delta\, t_i$, while N_i is equal to 1 when the source is variable. We adapted the calculation to our specific analysis and used the light curves for the evaluation of the DC. For each time bin in which the source is detected (i.e., TS > 4 or $N_{\mathrm{pred}} > 3$ or $\Delta\mathrm{Flux}/\mathrm{Flux} < 0.5$), we compared the flux to the "averaged subthreshold flux" (the flux averaged over 10 yr using the evaluation of spectral index reported in 1FLT). If the flux in the monthly time bin is above the "averaged subthreshold flux," we considered it in the calculation of the DC.

In our case the DC can be evaluated as $\mathrm{DC} = 100\frac{\sum_{i=0}^{n} N_i}{120}$ since Δt_i is 1 month for each source. We can calculate the DC for each source class independently of its redshift. We also calculated the duty cycle for each transient source class in the 4FGL using the same procedure adopted for the 1FLT. Since the light curves reported in the 4FGL have a time binning of 2 months, which is different from our sampling interval, we can only perform a qualitative comparison between the duty cycles of the 1FLT and 4FGL sources. In Figure 10 we compare between the average values of the DC for each transient source class in the 1FLT and the 4FGL catalogs. The 1FLT sources are characterized by a very low duty cycle. Clearly there is a selection effect due to the way that the 1FLT catalog was built because a bias was introduced by the definition of a significant point in the light-curve extraction. We can, however, obtain some qualitative insights about the difference between the DC of the radio galaxies and the blazar-like objects. In fact, the radio galaxy class has a greater DC than the FSRQ and BCU classes, which are characterized by shorter flaring episodes.

5.3. Discussion of Peculiar Sources

We discuss here some peculiar cases that deserve a detailed investigation and for which we built SEDs collecting all archival multiwavelength data[86] using the *SSDC-SED Tool*[87] and adding our data points for each of the TBINs.

5.3.1. Soft γ-Ray Blazars Detected with the Swift Burst Alert Telescope

Two 1FLT sources were also detected with the Swift Burst Alert Telescope (Krimm et al. 2013). The source 1FLT J0010 +1056 is associated with a Bayesian probability of 0.96 with Mrk 1501, which is reported as SWIFT J0010.5+1057 in the Swift-BAT 105-Month Hard X-ray Survey.[88] Mrk 1501 is an FSRQ located in the local universe at a redshift of $z = 0.089338$ (Sargent & Searle 1970). This source is the nearest FSRQ in the whole 1FLT sample. It was also reported by Arsioli & Polenta (2018). They searched for sources with short-lived γ-ray emission and found a TS ~ 26 for this source in just one monthly bin, that from 2010 June. We detected this

[86] https://tools.ssdc.asi.it/SED/docs/SED_catalogs_reference.html
[87] https://tools.ssdc.asi.it/SED/
[88] https://swift.gsfc.nasa.gov/results/bs105mon/

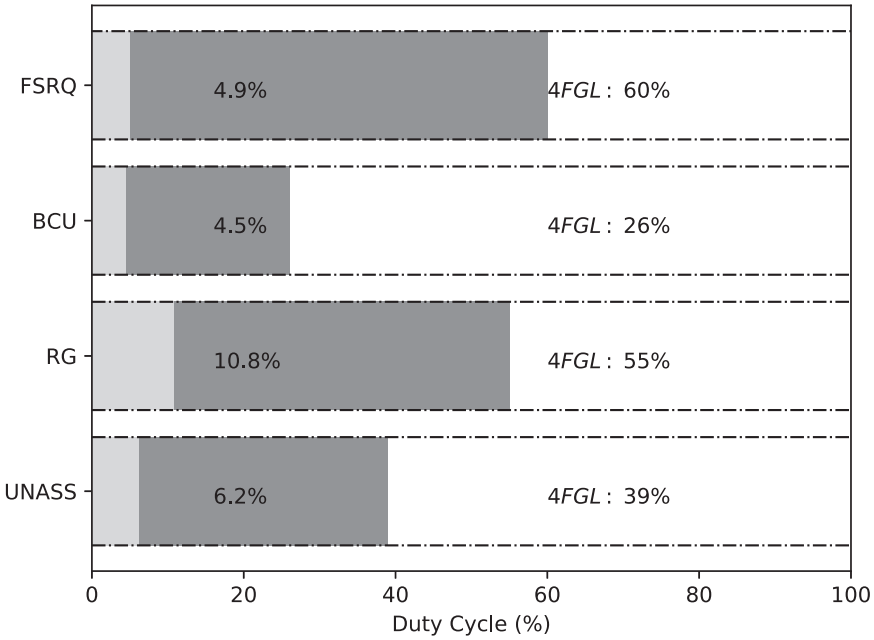

Figure 10. Average duty cycles for the different classes of objects from the 1FLT catalog compared to their values in the 4FGL catalog. The duty cycles of the 1FLT sources are shown in light gray with their numerical values in boldface. The duty cycles of the 4FGL sources are shown in dark gray with their numerical values labeled as such. The time binning of the light curves on which the duty cycle calculation is based is not the same for 1FLT and 4FGL: the 1FLT light curves are binned in 1-month intervals, while the 4FGL light-curve binning is 2 months.

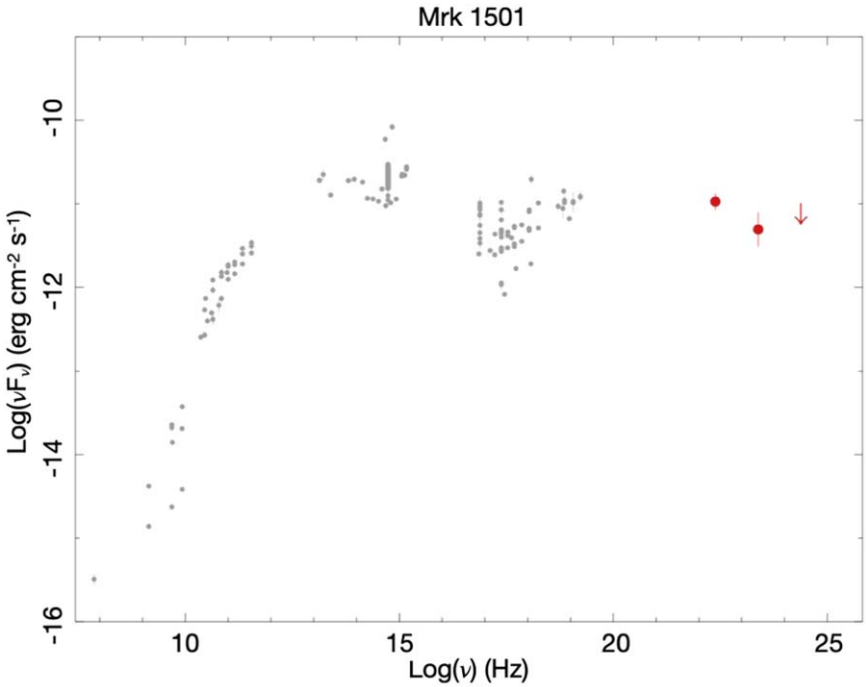

Figure 11. The SED of Mrk 1501 associated with 1FLT J0010+1056 detected in TBIN 21.5. The archival data points (see footnote 86) at other wavelengths are shown in gray. The γ-ray spectral data points for the corresponding 1FLT source are shown in red.

source in the TBIN 21.5 (2010 May 20 to June 20), thus confirming this short γ-ray flare from Mrk 1501.

The SED of Mrk 1501 is shown in Figure 11. The typical two-humped, blazar-like SED is clearly reproduced. Although the source was in a γ-ray flaring state, the Compton dominance (CD_γ), defined as the ratio of the inverse Compton to the synchrotron peak luminosity, is, in logarithmic scale, less than 1 as is typical of HSP BL Lacs (Abdo et al. 2010a; see Figure 22 in Giommi et al. 2012).

The source 1FLT J2010−2523 is associated with a Bayesian probability of 0.99 with PMN J2010−2524, a well-known FSRQ ($z = 0.825$, Massaro et al. 2015). It is also reported in the Swift-BAT 105-Month Hard X-ray Survey as SWIFT J2010.6 −2521 and as a γ-ray emitter by Paliya et al. (2019). We detected the source in several temporal bins. The first detection was in TBIN 6 (2009 February 3 to March 5), followed by a detection in TBINs 68 and 68.5 (2014 April 5 to May 20), and then from TBIN 72 to TBIN 73.5 (2014 August 5 to October 20).

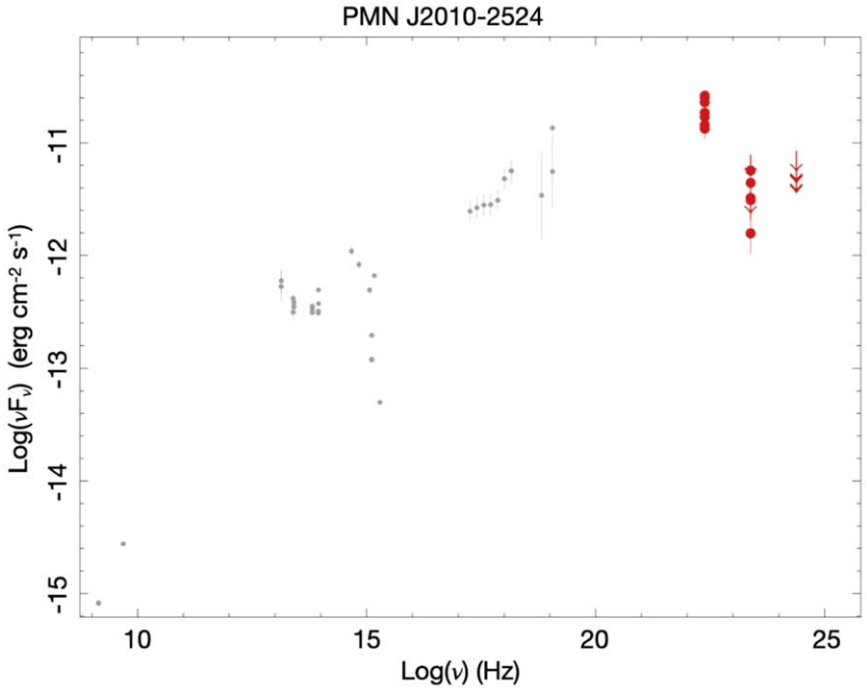

Figure 12. The SED of PMN J2010−2524 associated with 1FLT J2010−2523 detected in seven TBINs 6, 68, 68.5, 72, 72.5, 73, and 73.5. The archival data points (see footnote 86) at other wavelengths are shown in gray. The γ-ray spectral data points for the corresponding 1FLT (and for its different TBIN detections) source are shown in red.

The flaring activity of the source is quite evident in the light curve reported in Appendix C.

In contrast to Mrk 1501, the SED of PMN J2010−2524 has a CD_γ greater than 1, which is fairly common among FSRQs. The CD_γ can be seen in Figure 12.

5.3.2. Compact Steep-spectrum Source

1FLT J1416+3447 was detected in two consecutive and overlapping TBINs, TBIN 111.5 and TBIN 112 (2017 November 19 to 2018 January 4), which strengthens the reliability of the detection. It is associated, through the Bayesian method, with a probability of 0.85, with a radio CSS source, S4 1413+34. The SED of S4 1413+34 is shown in Figure 13.

CSS sources are thought to represent the first stages of evolution of the radio sources that eventually physically expand as Fanaroff-Riley I (FR I) or Fanaroff-Riley II (FR II) radio galaxies. The γ-ray emission in CSS sources was predicted by Stawarz et al. (2008), but these sources have proved to be elusive in the xFGL catalogs. Recently, Schulz et al. (2016) reported on the results of a dedicated analysis of PKS 2004 −447, which is associated with a γ-ray-loud young radio source that has a radio spectrum resembling that of a CSS and an optical spectrum that is like that of a narrow-line Seyfert 1. S4 1413+34, which does not have an optical identification, shows a core-jet structure at 5 GHz. The radio morphology (see Figure 9 of Dallacasa et al. 2013) shows a well-collimated jet, but the radio emission is dominated by the brightest compact component.

Abdo et al. (2010d) report on 11 misaligned AGNs detected at γ-ray energies, which, with the exception of NGC 1275, show no evidence for variability. Abdo et al. (2010d) suggested that sources with a larger CD, which are observed with a line of sight closer to the jet axis, are those preferentially detected with the Fermi-LAT (in contrast with what was found by Angioni et al. 2020). We evaluated the CD of S4 1413+34 at 5 GHz and obtained a value of CD = 0.28, which is consistent with the values previously found for the other misaligned AGNs. We conclude, therefore, that the observed γ-ray emission should be produced in the compact core region.

5.3.3. NGC 4278

1FLT J1219+2907 was detected in TBIN 7 (2009 March 5 to April 5) of our analysis; using the positional association procedure, we found that NGC 4278 lies within its error ellipse. The SED of NGC 4278 is shown in Figure 14. NGC 4278 ($z = 0.0021$) is a nearby galaxy identified as a likely radio compact symmetric object (CSO) with an FR I morphology. It shows a dominant, bright, flat-spectrum component identified as the core (see Figures 2M and 3M in Tremblay et al. 2016). From the north and south ends of the core, diffuse jets extend out to the west and east, respectively, creating an "S-shaped" symmetry as observed in other CSO radio sources. We calculated a CD of 0.71 at 366 5 GHz using the data reported in Schilizzi et al. (1983). This is a greater-than-average value of CD for an FR I, although it is reasonable for a γ-ray emitter.

Giroletti et al. (2005) reported that the source is oriented at a very small viewing angle ($2° < \theta < 4°$) with respect to the line of sight, although they did not find compelling evidence for strong beaming. They also proposed an alternative scenario in which the source could be oriented at a larger angle, with asymmetries related to the jet's interaction with the surrounding medium. NGC 4278 is optically classified as a low-luminosity and low-accreting AGN with a low-ionization nuclear emission-line region (LINER). All of these characteristics make

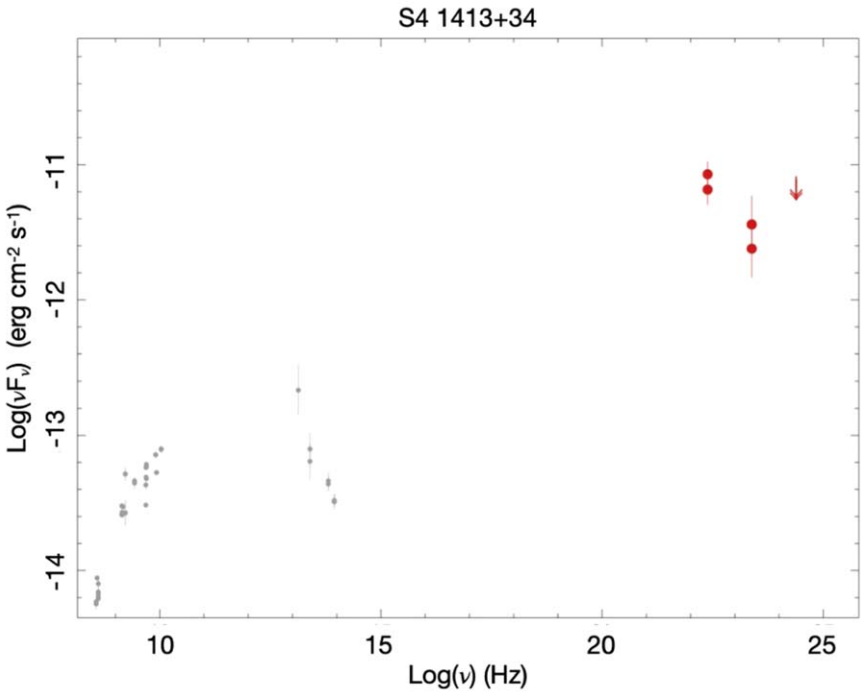

Figure 13. The SED of S4 1413+34 associated with 1FLT J1416+3447 detected in two different TBINs 111.5 and 112. The archival data points (see footnote 86) at other wavelengths are shown in gray. The γ-ray spectral data points for the corresponding 1FLT source (and for its different TBIN detections) are shown in red.

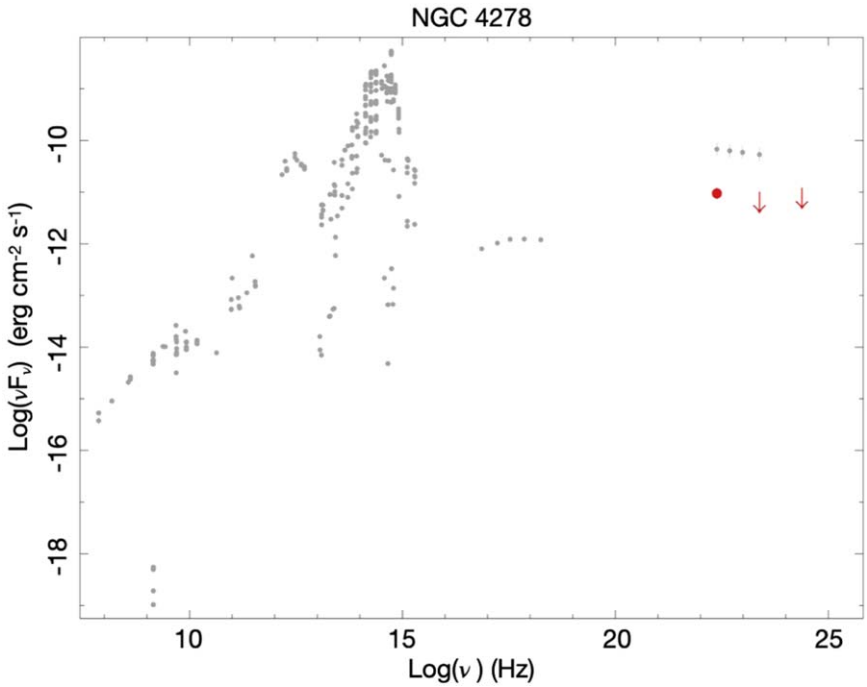

Figure 14. The SED of NGC 4278 associated with 1FLT J1219+2907 detected in TBIN 7. The archival data points (see footnote 86) at other wavelengths are shown in gray. The γ-ray spectral data points for the corresponding 1FLT source are shown in red. Gray data points at γ-ray frequency are AGILE data points.

NGC 4278 a very intriguing new type of γ-ray emitter. Until now, the detection of two CSOs, PKS 1718−649 (Migliori et al. 2016) and PMN J1603−4904 (Krauß et al. 2018), had been reported at γ-ray energies. Stawarz & Petrosian (2008) postulate, in their dynamical radiative model of young radio sources, that the γ-ray emission is produced via inverse Comptonization of circumnuclear (IR to UV) photon fields off relativistic electrons in compact, expanding lobes.

5.3.4. 3C 226

1FLT J0943+0940 is positionally consistent with 3C 226 and was detected in the TBIN 44 (2012 April 5 to May 5) of our analysis. 3C 226, located at $z = 0.818$ (Hewitt & Burbidge 1991), is an FR II radio galaxy (Laing et al. 1983) with an optical spectrum that shows the presence of narrow emission lines. The FR II radio morphology is clearly seen over

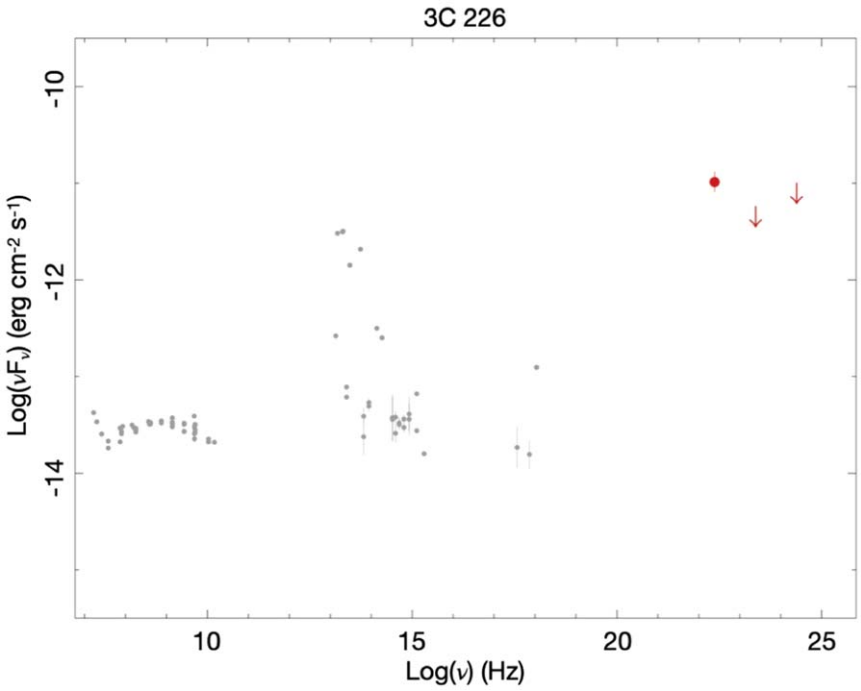

Figure 15. The SED of 3C 226 associated with 1FLT J0943+0940 detected in TBIN 44. The archival data points (see footnote 86) at other wavelengths are shown in gray. The γ-ray spectral data points for the corresponding 1FLT source are shown in red.

a span of 260 kpc (Best et al. 1997). The source has an asymmetric radio structure, having the southeastern lobe closer to the radio core than the northwestern lobe. However, when the radio and optical observations are combined, the source shows a large opening angle. It has a low CD of −2, which makes 3C 266 an unfavored candidate for γ-ray emission. Furthermore, it can be seen from the SED, which is shown in Figure 15, that there is a discrepancy between the archival data and the γ-ray data. FR II radio galaxies are, however, found to be variable from radio to γ-ray energies, e.g., 3C 111 in Grandi et al. (2012), whose variability has been postulated to be due to a new knot component ejected from the core. A similar scenario could be at play in 3C 226, which would strengthen the case for its association with 1FLT J0943+0940.

5.3.5. The Highest-redshift FSRQ: PMN J2219−2719

1FLT J2219−2732 is positionally consistent with PMN J2219 −2719 and was detected in TBIN 96 (2016 August 04 to 2016 September 04) of our analysis. PMN J2219−2719 is a well-known FSRQ belonging to the Fifth Roma-BZCAT catalog (Massaro et al. 2014) at a redshift of $z = 3.634$ (Hook et al. 2002). This source has a very low duty cycle (see Section 5.2) of about 2.5%, and it lies at the highest redshift of the entire 1FLT catalog. Examination of the SED (see Figure 16) reveals a large CD_γ of ∼1.8 during a period of flaring activity. This behavior is typical of FSRQs and is usually interpreted as an external Compton process (see Figure 11 of Abdo et al. 2010b). PMN J2219−2719 is also identified as the most distant TS > 25 blazar with monthly variability detected in Kreter et al. (2020). The other source with high redshift reported in Kreter et al. (2020), i.e., 5BZQ J0422−3844, is not detected with our method. The blind search undertaken with PGWave found several monthly seeds that were positionally compatible with this source but were discarded because they were located within 50′ of a 4FGL source.

6. Conclusions

In this work we have investigated the Fermi-LAT sky on monthly timescales to search for sources that are not detected when integrating on timescales of years and/or that are not already hosted in the Fermi-LAT xFGL general catalogs. We found the following:

1. The 1FLT catalog is mainly populated by soft sources with an average spectral index of ∼2.7 compared to ∼2.3 for the 4FGL-DR2. This confirms that these soft sources are not distinguishable from the diffuse γ-ray background when considered over multiyear integration times.
2. This study found that there are more FSRQs found when using a monthly binning compared to catalogs using data averaged over longer intervals. This is due both to BL Lacs that are in general less variable around 1 GeV and to FSRQs whose strong gamma-ray activity is mainly seen only during flaring events. If the flare intensity is fainter than the integrated background over years, we lose the capability to detect these FSRQs in long-time integrated catalogs.
3. In the 1FLT we detected sources only when they were in an active flaring phase. For this reason they show a high γ-ray luminosity with respect to the 4LAC sources whose fluxes were calculated over a longer integration time (see Figure 6).
4. The 1FLT sources show a fainter radio flux than the 4LAC FSRQs (see Figure 8), and they also have a very low duty cycle relative to 4FGL sources. This correlation between the radio-loudness and variability was already described in Romero et al. (1999) in the optical wave band.

In conclusion, the 1FLT catalog comprises 142 γ-ray sources, of which ∼70% are associated with soft AGN-type counterparts, principally BCU and FSRQ. Approximately 28% of 1FLT sources remain unassociated. This fraction is similar to

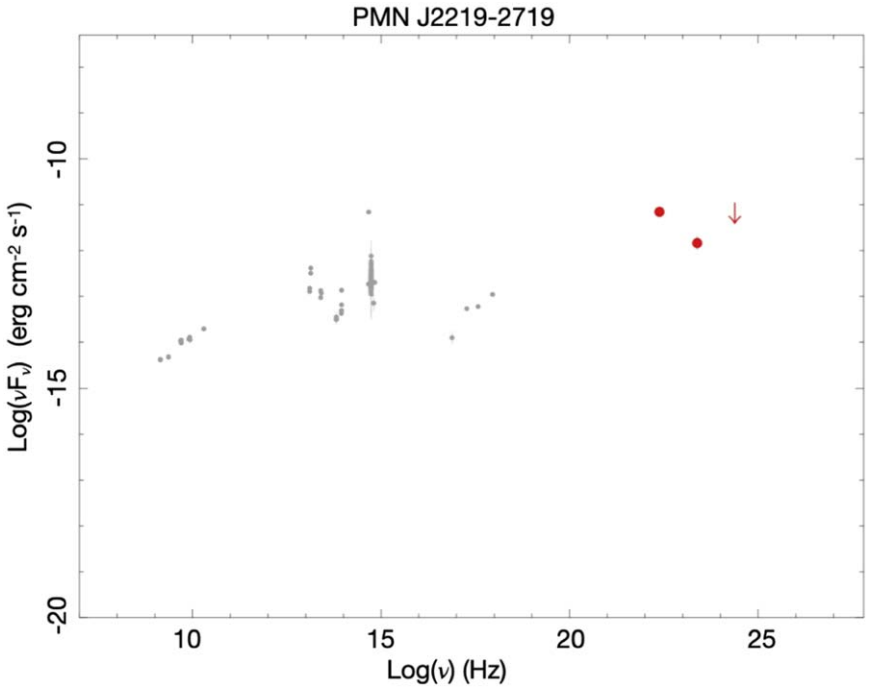

Figure 16. The SED of PMN J2219-2719 associated with 1FLT J2219-2732 detected in TBIN 96. The archival data points (see footnote 86) at other wavelengths are shown in gray. The γ-ray spectral data points for the corresponding 1FLT source are shown in red.

the percentage of unassociated sources found in the Fermi-LAT general catalogs. The 72 1FLT sources that have TS between 25 and 30 and are detected in only one of the monthly time bins should be regarded as low confidence, given their $\sim$34% probability of being statistical fluctuations. Out of the 142 monthly detections, we found only 4 correspondences with the 2FAV catalog whose analysis is on a 1 week time interval. This shows that integrating over different time intervals does not reproduce the same γ-ray sky and that the discovery space of Fermi-LAT remains large. The 1FLT catalog will be available online for an easy and fast visualization at www.ssdc.asi.it/fermi1flt.

The Fermi-LAT Collaboration acknowledges generous ongoing support from a number of agencies and institutes that have supported both the development and the operation of the LAT, as well as scientific data analysis. These include the National Aeronautics and Space Administration and the Department of Energy in the United States; the Commissariat à l'Energie Atomique and the Centre National de la Recherche Scientifique/Institut National de Physique Nucléaire et de Physique des Particules in France; the Agenzia Spaziale Italiana and the Istituto Nazionale di Fisica Nucleare in Italy; the Ministry of Education, Culture, Sports, Science and Technology (MEXT), High Energy Accelerator Research Organization (KEK), and Japan Aerospace Exploration Agency (JAXA) in Japan; and the K. A. Wallenberg Foundation, the Swedish Research Council, and the Swedish National Space Board in Sweden.

Additional support for science analysis during the operations phase is gratefully acknowledged from the Istituto Nazionale di Astrofisica in Italy and the Centre National d'Études Spatiales in France. This work was performed in part under DOE contract DE-AC02-76SF00515. S.B. acknowledges financial support by the European Research Council for the ERC Starting grant MessMapp, under contract No. 949555. G.T. acknowledges support from grant ASI/INAF n.2015-023-R.1. This work has been partially supported by the EOSC-hub EU project G.A 777536, and special thanks go to Daniele Spiga (INFN Perugia) and Mirko Mariotti (University of Perugia) for help with the computing infrastructure.

Additional support for science analysis during the operations phase is gratefully acknowledged from Space Science Data Center Tools,[89] Open Universe portal, and VOU-Blazar Tool (see footnote 83) (Giommi et al. 2019, 2020). Special thanks are due to Benoit Lott who contributed to the source association, and to the members of the Fermi-LAT collaboration who have provided their help in every step of this work.

Facility: Fermi-LAT.

Software: PGWave tool (Ciprini et al. 2007), Fermipy (v0.18.0; Wood et al. 2017), Fermitools (v1.2.1; Fermi Science Support Development Team 2019).

Appendix A
Description of the FITS Version of the 1FLT Catalog

The FITS format version of the 1FLT catalog has three binary table extensions. The extension `SOURCES` has all of the information about the sources. Its format is described in Table A1.

The extension `FLARES` contains the information about all the monthly detections, including multiple monthly flares of the same 1FLT source reported with the same assigned number. It includes also SED data points. Its format is described in Table A2.

The extension `EnergyBounds` contains the definitions of the bands in which the SED data points were computed and the settings of the analysis. Its format is described in Table A3.

[89] https://www.asdc.asi.it/

Table A1
Catalog Table SOURCES Description

Column	Description
Source_Name	1FLT JHHMM+DDMM, according to IAU specifications for nomenclature.
SRCNUM	Source number. It is the same for multiple flares of the same source
TBIN_1m	Time bin in which the source was detected with the greatest TS, where 0–119 stand for the first 120 months starting 2018 August 4 UTC (MET 239557417), 0.5–119.5 stands for the shifted 120 months starting 2018 August 19 UTC (MET 240846000)
Flares	Number of flares of this source
RAJ2000	R.A., J2000, in degrees
DEJ2000	Decl., J2000, in degrees
GLON	Galactic longitude, in degrees
GLAT	Galactic latitude, in degrees
Conf_95_SemiMajor	Semimajor axis of the error ellipse at 95% confidence, in degrees
Conf_95_SemiMinor	Semiminor axis of the error ellipse at 95% confidence, in degrees
Conf_95_PosAng	Position angle of the 95%-confidence semimajor axis, from celestial north, positive toward Increasing R.A. (eastward), in degrees
Test_Statistic	Likelihood test statistic for 100 MeV–300 GeV analysis
Npred	Number of predicted events in the model
PL_Index	Photon index for the PowerLaw fit
Unc_PL_Index	1σ error on PL_Index
Flux	Integral photon flux in the 100 MeV–300 GeV range, in photons cm^{-2} s^{-1}
Unc_Flux	1σ error on flux, in photons cm^{-2} s^{-1}
Energy_Flux	Energy flux in MeV cm^{-2} s^{-1}, in the 100 MeV–300 GeV range
Unc_Energy_Flux	1σ error on Energy_Flux, in MeV cm^{-2} s^{-1}
ASSOC_FERMI	Correspondence to Fermi-LAT xFGL and FL8Y catalog
ASSOC_GAM	Correspondence to γ-ray source catalog
ASSOC_FAVA	Correspondence to 2FAV source catalog
LMC	True if the source is in the LMC region
CenA	True if the source is near Cen A
Class	Class of the most likely counterpart. See also Section 3.1
Assoc_Name	Designation of the most likely associated counterpart
Assoc_Prob_Bay	Probability of association according to the Bayesian method. It is set to 0 for point sources with only positional association (see Section 3)
Assoc_RA	Most likely counterpart R.A., J2000, in degrees
Assoc_Dec	Most likely counterpart decl., J2000, in degrees
Redshift	Most likely counterpart redshift
Radio_Flux	1.4 GHz most likely counterpart flux density; units: mJy
log10(Nu_Peak)	Log10 synchrotron peak frequency measured with a third-degree polynomial fit function; units: Hz (Ackermann et al. 2015)
Low_Confidence	True if a source has a TS < 30 and only one monthly detection

(This table is available in its entirety in FITS format.)

Table A2
Catalog Table FLARES Description

Column	Description
SRCNUM	Multiple monthly flares of the same 1FLT source have the same assigned number
repROI	True if the source is detected in multiple overlapping ROI
repTBIN	True if the source is detected in more than one TBIN
TBIN_1m	See Table A1
TSTART	Beginning of observation time window in MET seconds
TSTOP	End of observation time window in MET seconds
RAJ2000	See Table A1
DEJ2000	See Table A1
GLON	See Table A1
GLAT	See Table A1
Conf_95_SemiMajor	See Table A1
Conf_95_SemiMinor	See Table A1
Conf_95_PosAng	See Table A1
Test_Statistic	See Table A1
Npred	See Table A1
PL_Index	See Table A1
Unc_PL_Index	See Table A1
Flux	See Table A1
Unc_Flux	See Table A1
Energy_Flux	See Table A1
Unc_Energy_Flux	See Table A1
nuFnu_band	SED data points in three energy bands, as reported in Table A3, in MeV cm^{-2} s^{-1}
nuFnu_ul_band	SED data points upper limits at 2σ confidence in three energy bands, as reported in Table A3, in MeV cm^{-2} s^{-1}
Unc_nuFnu_band	1σ error on SED data points in three energy bands, as reported in Table A3, in MeV cm^{-2} s^{-1}
Test_Statistic_band	SED data point test statistic in three energy bands, as reported in Table A3

Table A3
Catalog Table EnergyBounds Description

Column	Description
LowerEnergy	Value of the minimum energy, in MeV
UpperEnergy	Value of the maximum energy, in MeV
ENumBins	Bins per decade in energy
EvType	LAT event class
ZenithCut	Zenith angle cut, in deg
PixelSize	Binning in space, in deg

Appendix B
Source Lists

Table B1 contains the complete 1FLT source list but only a subset of the columns reported in the extension SOURCES of the FITS format version of the catalog. Tables B2 and B3 contain, respectively, the Sun and the GRB detection lists.

Table B1
Catalog Table: See the Description of the Columns in Table A1

1FLT Source Name	SRC NUM	TBIN 1m	Flares	RAJ2000 (deg)	DEJ2000 (deg)	Conf 95 SemiMaj (deg)	Conf 95 SemiMin (deg)	Conf 95 PosAng (deg)	TS	PL Index	Flux (photons cm^{-2} s^{-1})	Class	Assoc Name	Low Conf
J0002−2148	1	118.5	1	0.5	−21.81	0.18	0.14	115	43	1.8 ± 0.2	1.5E-8 ± 6.1E-9	bcu	PKS 2359−221	false
J0010+1056	2	21.5	1	2.53	10.94	0.31	0.24	140	38	2.5 ± 0.2	8.3E-8 ± 2.3E-8	fsrq	Mrk 1501	false
J0010+3905	3	16	1	2.7	39.09	0.57	0.46	91	33	3.4 ± 0.3	1.1E-7 ± 2.4E-8	bcu	GB6 J0008+3856	false
J0112+0711	4	34	1	18.21	7.2	0.46	0.29	2	25	2.3 ± 0.3	4.1E-8 ± 1.7E-8	unass		true
J0115+5230	5	59	1	18.86	52.51	0.23	0.19	138	26	2.1 ± 0.2	3.7E-8 ± 1.8E-8	unass		true
J0115−2237	6	19.5	1	18.96	−22.63	0.3	0.25	4	30	2.1 ± 0.2	3.7E-8 ± 1.8E-8	unass		false
J0121+2602	7	73.5	2	20.4	26.04	0.56	0.45	105	33	3 ± 0.3	1.3E-7 ± 3.4E-8	fsrq	TXS 0120+259	false
J0125+2212	8	55.5	1	21.46	22.22	0.62	0.49	129	26	3.1 ± 0.3	1E-7 ± 2.9E-8	bcu	TXS 0122+220	true
J0136+1505	9	56.5	1	24.16	15.09	0.65	0.41	139	27	2.9 ± 0.3	7.7E-8 ± 2.1E-8	bcu	TXS 0133+146	true
J0139+1744	10	10.5	1	24.83	17.74	0.25	0.19	138	28	2.1 ± 0.2	2.6E-8 ± 1.2E-8	fsrq	PKS 0136+176	true
J0141−1330	11	106.5	2	25.42	−13.51	0.2	0.18	132	54	2.1 ± 0.2	3.7E-8 ± 1.1E-8	bcu	TXS 0139−138	false
J0149+2602	12	51	1	27.34	26.04	0.83	0.58	67	31	3.1 ± 0.3	1E-7 ± 2.6E-8	fsrq	TXS 0145+256	false
J0202+3910	13	33.5	1	30.6	39.17	0.58	0.52	134	26	3 ± 0.3	7.6E-8 ± 2.1E-8	unass		true
J0209+7459	14	4.5	1	32.38	74.99	0.85	0.68	93	27	3.2 ± 0.2	1.4E-7 ± 3.7E-8	bcu	GB6 J0214+7437	true
J0230+1423	15	85.5	1	37.64	14.39	0.67	0.64	79	28	3.4 ± 0.4	1.4E-7 ± 3.4E-8	unass		true
J0240−4657	16	21.5	2	40.16	−46.95	0.62	0.42	73	35	2.8 ± 0.3	9.9E-8 ± 2.6E-8	unass		false
J0240−4739	17	101	1	40.22	−47.66	1.55	0.64	44	29	3.6 ± 0.4	7.5E-8 ± 1.7E-8	bcu	PMN J0240−4822	true
J0253+1801	18	9	1	43.38	18.02	0.7	0.58	82	27	2.9 ± 0.2	1.1E-7 ± 2.7E-8	bcu	PKS 0250+178	true
J0259-5406	19	64.5	1	44.84	−54.1	0.45	0.44	86	28	2.9 ± 0.3	5.5E-8 ± 1.6E-8	unass		true
J0321−1136	20	85.5	1	50.29	−11.61	0.49	0.32	61	30	2.6 ± 0.2	6.7E-8 ± 2E-8	bcu	TXS 0318−115	false
J0332−1733	21	111	1	53.03	−17.56	0.27	0.24	107	27	2.5 ± 0.3	5.1E-8 ± 1.9E-8	bcu	PMN J0332−1734	true
J0342−1807	22	45	1	55.53	−18.12	0.58	0.84	83	28	3.1 ± 0.3	7.6E-8 ± 1.9E-8	bcu	TXS 0340−182	true
J0343+1200	23	116	1	55.76	12.0	0.46	0.34	29	29	2.5 ± 0.2	1.9E-7 ± 6.3E-8	unass		true
J0350+0512	24	90	1	57.68	5.2	0.34	0.22	56	31	2.3 ± 0.2	7.1E-8 ± 2.4E-8	bcu	TXS 0348+049	false
J0357−1509	25	50	1	59.4	−15.15	0.92	0.67	148	28	3.8 ± 0.6	9E-8 ± 2.2E-8	unass		true
J0402−1227	26	72	1	60.51	−12.46	0.55	0.47	4	26	3 ± 0.3	9E-8 ± 2.8E-8	unass		true
J0402+1431	27	100.5	1	60.66	14.52	0.77	0.66	44	34	4.1 ± 0.6	1.6E-7 ± 3.5E-8	unass		false
J0408+6839	28	73	1	62.15	68.66	0.34	0.28	49	27	2.4 ± 0.2	7.3E-8 ± 2.2E-8	bcu	TXS 0402+682	true
J0409−5530	29	83	1	62.29	−55.5	0.93	0.73	145	30	3.5 ± 0.4	8.1E-8 ± 1.9E-8	unass		false
J0448−3424	30	100.5	1	72.15	−34.41	0.17	0.15	16	49	2.1 ± 0.2	3.7E-8 ± 1.3E-8	bcu	TXS 0447−345	false
J0457−6830	31	63	1	74.3	−68.51	0.36	0.29	136	29	2.8 ± 0.3	8.1E-8 ± 2.2E-8	unass		true
J0459−7909	32	80	2	75.0	−79.16	0.84	0.8	30	31	4.1 ± 0.6	1E-7 ± 2.3E-8	bcu	PKS 0509−792	false
J0512−7007	33	30	1	78.05	−70.13	0.52	0.43	117	32	2.8 ± 0.3	9.6E-8 ± 2.7E-8	unass		false
J0519−3709	34	116	1	79.94	−37.16	0.81	0.36	72	60	3 ± 0.2	1E-7 ± 1.8E-8	bcu	SUMSS J051941−371449	false
J0520−6726	35	35.5	1	80.04	−67.44	0.66	0.43	42	41	2.7 ± 0.2	1.1E-7 ± 2.6E-8	unass		false
J0527−3747	36	37.5	1	81.8	−37.79	1.16	0.89	105	33	4.1 ± 0.5	1.2E-7 ± 2.6E-8	unass		false
J0546+8247	37	41	2	86.54	82.79	0.42	0.28	40	31	2.2 ± 0.2	3.8E-8 ± 1.2E-8	bcu	S5 0532+82	false
J0620−1226	38	97.5	1	95.14	−12.44	0.63	0.44	84	26	2.7 ± 0.2	8.1E-8 ± 2.6E-8	agn	TXS 0617−123	true
J0642−3237	39	48	1	100.52	−32.63	0.87	0.51	93	31	3.4 ± 0.3	1.1E-7 ± 2.5E-8	bcu	PKS 0641−331	false
J0645+7222	40	6.5	1	101.27	72.38	1.0	0.83	15	36	4 ± 0.6	1.2E-7 ± 2.4E-8	bcu	GB6 J0642+7215	false
J0653−3649	41	100.5	1	103.47	−36.83	0.26	0.21	139	25	2.3 ± 0.3	4.6E-8 ± 2.1E-8	bcu	NVSS J065356−365202	true
J0657+4619	42	112.5	1	104.39	46.33	0.76	0.56	63	28	3.4 ± 0.4	9.8E-8 ± 2.4E-8	rg	B3 0653+464	true
J0657−5348	43	104	2	104.44	−53.8	0.19	0.17	151	60	2.3 ± 0.2	6.8E-8 ± 1.7E-8	bcu	PMN J0657−5406	false
J0724+7027	44	100.5	1	111.01	70.45	0.34	0.25	96	47	2.5 ± 0.2	6.3E-8 ± 1.6E-8	bcu	87 GB 071829.7+701845	false
J0734−6137	45	56	2	113.66	−61.62	1.02	0.66	117	27	3.5 ± 0.4	1.1E-7 ± 2.7E-8	bcu	PMN J0734−6122	false
J0734+1721	46	109	1	113.7	17.36	0.5	0.5	0	29	2.5 ± 0.2	7.4E-8 ± 2.2E-8	unass		true

Table B1
(Continued)

1FLT Source Name	SRC NUM	TBIN 1m	Flares	RAJ2000 (deg)	DEJ2000 (deg)	Conf 95 SemiMaj (deg)	Conf 95 SemiMin (deg)	Conf 95 PosAng (deg)	TS	PL Index	Flux (photons cm^{-2} s^{-1})	Class	Assoc Name	Low Conf
J0804+8311	47	66	1	121.25	83.2	0.96	0.72	124	34	3.5 ± 0.3	8.4E-8 ± 1.9E-8	fsrq	S5 0740+82	false
J0837+2500	48	112.5	1	129.43	25.01	0.21	0.17	0	41	1.8 ± 0.2	2E-8 ± 8.9E-9	fsrq	B2 0834+25	false
J0845+5040	49	35.5	1	131.33	50.67	0.5	0.5	0	25	3.4 ± 0.4	7.9E-8 ± 2E-8	bcu	TXS 0843+510	true
J0855−1233	50	111	1	133.75	−12.56	0.94	0.6	178	25	3.3 ± 0.3	8.3E-8 ± 2.1E-8	unass		true
J0902+3323	51	62.5	1	135.66	33.39	0.6	0.3	130	25	2.6 ± 0.3	4.9E-8 ± 1.9E-8	bcu	VLSS J0900.5+3330*	true
J0943+0940	52	44	1	145.81	9.68	0.92	1.2	81	31	3.4 ± 0.4	1.2E-7 ± 2.8E-8	rg	3C 226	false
J0953−3006	53	116	5	148.37	−30.11	0.24	0.18	138	39	2.3 ± 0.2	4.1E-8 ± 1.2E-8	bcu	PMN J0952−3006	false
J1008+1319	54	34	1	152.1	13.33	0.5	0.34	5	29	2.3 ± 0.2	5.7E-8 ± 2.1E-8	agn	GB6 J1009+1322	true
J1008+0528	55	66.5	1	152.14	5.47	1.17	0.5	84	27	2.8 ± 0.3	1E-7 ± 3.1E-8	fsrq	TXS 1006+056	true
J1016+0959	56	87.5	1	154.04	9.99	0.83	0.7	61	25	3.9 ± 0.5	9.1E-8 ± 2.3E-8	bcu	4C +09.36	true
J1019−3216	57	48.5	1	154.95	−32.28	0.55	0.43	143	30	2.8 ± 0.2	8.8E-8 ± 2.4E-8	ssrq	TXS 1018−319	true
J1022−3140	58	74.5	1	155.74	−31.67	0.32	0.26	176	25	2.1 ± 0.3	3.1E-8 ± 1.5E-8	unass		true
J1053+1409	59	89	1	163.35	14.16	0.7	0.63	144	33	3.1 ± 0.3	1.1E-7 ± 2.5E-8	fsrq	TXS 1051+147	false
J1053+1529	60	19.5	1	163.46	15.5	0.66	0.6	84	25	3.2 ± 0.4	8.4E-8 ± 2.4E-8	fsrq	GB6 J1054+1507	true
J1055+6509	61	80.5	2	163.97	65.16	0.18	0.17	18	57	2.4 ± 0.2	5.3E-8 ± 1.4E-8	bcu	GB6 J1055+6509	false
J1112−0934	62	108	1	168.08	−9.57	0.26	0.24	100	29	2.3 ± 0.3	5.3E-8 ± 2.4E-8	bcu	TXS 1109−093	true
J1113−0537	63	83	1	168.36	−5.63	0.49	0.43	114	25	3 ± 0.3	8.5E-8 ± 2.4E-8	unass		true
J1117+8436	64	89.5	1	169.28	84.61	0.52	0.47	61	25	2.9 ± 0.3	6.7E-8 ± 1.9E-8	unass		true
J1117−4839	65	14	2	169.39	−48.66	0.19	0.18	111	62	2.4 ± 0.2	1.1E-7 ± 2.8E-8	bcu	CRATES J1117−4838	false
J1117−1604	66	74	1	169.45	−16.08	0.52	0.31	26	27	2.4 ± 0.2	6E-8 ± 2E-8	bcu	PMN J1117−1609	true
J1133−1052	67	7.5	1	173.43	−10.87	0.2	0.17	128	36	2 ± 0.2	2.7E-8 ± 1.1E-8	bcu	NVSS J113347−105640	false
J1137+1010	68	54	1	174.35	10.17	0.27	0.25	147	26	2.3 ± 0.3	4.1E-8 ± 1.8E-8	bcu	TXS 1136+106	true
J1141+0023	69	51.5	1	175.41	0.39	0.23	0.19	125	36	2.1 ± 0.2	3.2E-8 ± 1.2E-8	fsrq	PMN J1141+0022	false
J1145−4044	70	67.5	1	176.27	−40.75	0.62	0.48	90	26	2.8 ± 0.3	9.5E-8 ± 2.8E-8	bcu	SUMSS J114604−405932	true
J1145−1531	71	41	2	176.39	−15.53	0.28	0.22	140	39	2.4 ± 0.2	6.3E-8 ± 1.8E-8	bcu	TXS 1143−152	false
J1146−0926	72	102	3	176.6	−9.45	0.18	0.16	96	110	2.5 ± 0.1	1.4E-7 ± 2.4E-8	bcu	PMN J1146−0932	false
J1151+3938	73	98.5	1	177.91	39.64	0.46	0.35	29	25	2.1 ± 0.2	3E-8 ± 1.4E-8	fsrq	GB6 J1151+4008	true
J1153−3658	74	74.5	1	178.42	−36.97	0.26	0.25	109	26	2.3 ± 0.2	5.5E-8 ± 2.2E-8	bcu	PKS 1150−369	true
J1201−2658	75	104	1	180.43	−26.98	0.64	0.58	133	30	3.1 ± 0.3	7.6E-8 ± 1.7E-8	bcu	TXS 1200−261	true
J1202−2144	76	46	1	180.73	−21.74	0.54	0.81	69	25	2.8 ± 0.3	7.4E-8 ± 2.1E-8	unass		true
J1210+3708	77	13	1	182.58	37.14	0.38	0.38	37	29	2.7 ± 0.3	6.4E-8 ± 2.3E-8	fsrq	B3 1206+374	true
J1219+2907	78	7	1	184.9	29.12	0.5	0.5	0	25	3.3 ± 0.4	9.8E-8 ± 3.1E-8	rg	NGC 4278	true
J1223−0847	79	26	1	185.93	−8.78	0.37	0.3	147	28	2.5 ± 0.2	8.7E-8 ± 3.2E-8	bcu	PMN J1223−0907	true
J1224−0536	80	8	2	186.16	−5.6	0.44	0.23	48	42	2.2 ± 0.2	4.7E-8 ± 1.4E-8	bcu	NVSS J122430−053030	false
J1226+0232	81	47	1	186.51	2.54	0.37	0.26	50	50	2.9 ± 0.2	1.6E-7 ± 3.9E-8	bcu	PMN J1225+0235	false
J1237−4430	82	104	1	189.48	−44.51	0.48	0.34	57	29	2.8 ± 0.2	9E-8 ± 2.6E-8	unass		true
J1259+5444	83	58.5	1	194.96	54.74	0.5	0.5	0	27	3 ± 0.3	6.9E-8 ± 1.7E-8	fsrq	VLSS J1259.3+5432	true
J1322−4521	84	6	1	200.7	−45.36	1.22	1.07	131	26	3.1 ± 0.3	1.3E-7 ± 3.3E-8	unass		true
J1323−4439	85	86.5	2	200.9	−44.67	0.31	0.23	146	26	2.4 ± 0.2	6.5E-8 ± 2.4E-8	fsrq	PKS 1320−446	false
J1331+1346	86	103.5	1	202.84	13.77	0.26	0.2	108	38	2 ± 0.2	2.9E-8 ± 1.2E-8	bcu	NVSS J133134+135227	false
J1356−1545	87	21.5	2	209.1	−15.77	0.36	0.31	139	29	2.6 ± 0.2	6.8E-8 ± 1.9E-8	fsrq	PMN J1357−1527	false
J1402−1547	88	96	1	210.72	−15.79	0.72	0.59	125	29	3.1 ± 0.2	1.3E-7 ± 3.6E-8	bcu	PMN J1404−1538	true
J1412+7641	89	27.5	1	213.2	76.69	0.45	0.31	0	33	2.6 ± 0.2	5.1E-8 ± 1.3E-8	bcu	NVSS J141134+763515	false
J1416+3447	90	111.5	2	214.07	34.8	0.24	0.21	159	47	2.5 ± 0.2	6.4E-8 ± 1.9E-8	css	S4 1413+34	false
J1419+3708	91	59.5	2	214.76	37.14	0.71	0.62	65	36	3.2 ± 0.4	7.7E-8 ± 1.7E-8	fsrq	B3 1417+375	false
J1421−2222	92	37.5	1	215.41	−22.38	0.23	0.2	64	27	2.3 ± 0.2	4.4E-8 ± 1.8E-8	bcu	PMN J1421−2221	true

Table B1
(Continued)

1FLT Source Name	SRC NUM	TBIN 1m	Flares	RAJ2000 (deg)	DEJ2000 (deg)	Conf 95 SemiMaj (deg)	Conf 95 SemiMin (deg)	Conf 95 PosAng (deg)	TS	PL Index	Flux (photons cm^{-2} s^{-1})	Class	Assoc Name	Low Conf
J1422−3254	93	28	1	215.67	−32.9	1.0	0.91	27	27	2.6 ± 0.2	7.9E-8 ± 2.2E-8	bcu	PKS 1421−322	true
J1426+3139	94	113	1	216.75	31.66	0.7	0.53	118	26	2.3 ± 0.3	5.8E-8 ± 2.1E-8	bcu	TXS 1423+323	true
J1502−2420	95	107.5	1	225.73	−24.34	0.31	0.23	140	33	2.5 ± 0.2	8.6E-8 ± 2.4E-8	unass		false
J1513−2830	96	70	2	228.4	−28.5	0.17	0.21	161	66	2.4 ± 0.2	8.6E-8 ± 2E-8	bcu	PMN J1512−2828	false
J1522+1535	97	27	1	230.6	15.6	0.51	0.31	23	26	2.5 ± 0.2	7E-8 ± 2.5E-8	fsrq	SDSS J152247.54+153520.8	true
J1528−1348	98	91.5	1	232.22	−13.8	0.41	0.27	38	42	2.8 ± 0.2	1.2E-7 ± 2.8E-8	bcu	TXS 1527−135	false
J1533−2130	99	98	3	233.45	−21.5	0.18	0.16	118	37	2.1 ± 0.2	5.2E-8 ± 1.9E-8	unass		false
J1544+2705	100	77.5	1	236.04	27.1	1.35	0.78	137	30	2.4 ± 0.2	5E-8 ± 1.8E-8	unass		false
J1554−0252	101	109	2	238.56	−2.87	0.23	0.18	77	41	2.3 ± 0.2	8.5E-8 ± 2.4E-8	bcu	PMN J1554−0239	false
J1605+7725	102	91.5	2	241.37	77.42	0.38	0.26	121	40	2.5 ± 0.2	6E-8 ± 1.5E-8	bcu	VLSS J1606.2+7658	false
J1618−1016	103	101.5	1	244.57	−10.28	0.3	0.22	61	27	2.2 ± 0.2	5.2E-8 ± 1.9E-8	bcu	TXS 1615−102	true
J1622+0044	104	30	1	245.71	0.74	0.43	0.25	54	27	2.3 ± 0.3	5.6E-8 ± 2.4E-8	unass		true
J1626+5436	105	86.5	2	246.51	54.61	0.24	0.2	13	60	2.7 ± 0.2	8.9E-8 ± 2E-8	fsrq	CRATES J1626+5442	false
J1628−1449	106	110.5	1	247.05	−14.82	0.26	0.22	171	25	2.2 ± 0.2	5.4E-8 ± 2.5E-8	bcu	PKS 1625−149	true
J1649+2725	107	4.5	1	252.49	27.42	0.94	0.85	169	28	4.2 ± 0.7	9.3E-8 ± 2.1E-8	bll	B2 1645+27	true
J1701+2801	108	0.5	1	255.42	28.02	0.31	0.25	56	27	2.6 ± 0.3	5.4E-8 ± 1.8E-8	unass		true
J1708−1246	109	72	2	257.14	−12.78	0.19	0.15	162	39	2.1 ± 0.1	4.3E-8 ± 1.3E-8	bcu	NVSS J170822−124426	false
J1732+1510	110	71.5	2	263.2	15.17	0.31	0.26	152	46	2.9 ± 0.2	8E-8 ± 1.7E-8	bcu	TXS 1731+152A	false
J1734+5158	111	84.5	1	263.61	51.97	0.63	0.43	53	45	3.3 ± 0.3	1.5E-7 ± 3.1E-8	bcu	TXS 1734+516	false
J1737+1854	112	42	1	264.27	18.9	0.29	0.23	100	28	2.4 ± 0.3	5.4E-8 ± 2.3E-8	unass		true
J1752+4355	113	119.5	1	268.2	43.92	0.28	0.27	94	26	2.5 ± 0.3	4.1E-8 ± 1.6E-8	fsrq	S4 1751+44	true
J1801−7816	114	32.5	2	270.31	−78.27	0.28	0.23	129	55	2.6 ± 0.2	1.3E-7 ± 2.8E-8	bcu	PKS 1754−782	false
J1803+2523	115	13.5	1	270.84	25.4	0.35	0.28	32	32	2.6 ± 0.2	8.9E-8 ± 2.5E-8	bcu	TXS 1801+253	false
J1815+2017	116	83.5	2	273.95	20.29	0.42	0.3	120	29	2.9 ± 0.3	1.1E-7 ± 3.2E-8	unass		false
J1823+4759	117	71.5	1	275.82	48.0	0.5	0.5	0	25	3 ± 0.3	9.4E-8 ± 2.4E-8	bcu	TXS 1821+483	true
J1851−6844	118	5	1	282.83	−68.74	0.25	0.19	156	47	2.4 ± 0.2	8.7E-8 ± 2.6E-8	bcu	PKS 1847−688	false
J1918−2816	119	27.5	1	289.63	−28.27	0.7	0.67	142	30	3.2 ± 0.3	1.6E-7 ± 4E-8	bcu	PMN J1919−2823	true
J1919−4543	120	21	2	289.84	−45.73	0.26	0.22	34	41	2.6 ± 0.2	8.2E-8 ± 2.1E-8	fsrq	PKS 1915−458	false
J1922−6615	121	90.5	1	290.61	−66.25	0.34	0.25	97	27	2.5 ± 0.2	5.8E-8 ± 2E-8	unass		true
J1929−7909	122	34.5	2	292.36	−79.15	0.35	0.27	138	36	2.7 ± 0.2	1E-7 ± 2.8E-8	bcu	PMN J1931−7930	false
J1933−5420	123	101	1	293.42	−54.34	0.5	0.5	0	27	2.8 ± 0.2	8.5E-8 ± 2.2E-8	unass		true
J1936+5341	124	20.5	1	294.21	53.69	0.16	0.14	70	41	2 ± 0.2	3E-8 ± 1.1E-8	bcu	TXS 1935+536	false
J1937−5509	125	99.5	2	294.28	−55.15	0.18	0.15	81	80	2.2 ± 0.1	8.1E-8 ± 1.7E-8	bcu	PMN J1936−5512	false
J1943−3034	126	40.5	1	295.91	−30.57	0.8	0.47	148	28	3 ± 0.2	1E-7 ± 2.7E-8	unass		true
J1944−5135	127	99	1	296.12	−51.6	0.34	0.28	106	26	2.6 ± 0.2	6E-8 ± 2.1E-8	unass		true
J1952+4942	128	110	2	298.01	49.7	0.43	0.33	42	30	2.6 ± 0.2	8E-8 ± 2.5E-8	fsrq	TXS 1951+498	false
J2010−2523	129	72.5	7	302.56	−25.4	0.17	0.15	109	177	2.9 ± 0.1	2.3E-7 ± 2.6E-8	fsrq	PMN J2010−2524	false
J2013−1732	130	55.5	1	303.5	−17.55	0.5	0.5	0	27	3.2 ± 0.3	1.3E-7 ± 3.2E-8	unass		true
J2035−2708	131	55	1	308.76	−27.14	0.62	0.5	82	26	3 ± 0.2	1.1E-7 ± 3.4E-8	bcu	CRATES J2035−2632	true
J2035+0955	132	73.5	1	308.9	9.92	0.5	0.5	0	30	2.8 ± 0.2	1.2E-7 ± 3.2E-8	unass		false
J2112−3207	133	0	1	318.1	−32.12	0.74	0.43	94	43	2.9 ± 0.2	1.2E-7 ± 2.6E-8	bcu	PKS 2108−326	false
J2113−2616	134	71.5	1	318.37	−26.27	0.5	0.5	0	31	4.1 ± 0.6	1.5E-7 ± 3.4E-8	unass		false
J2114+1113	135	60.5	2	318.51	11.22	0.19	0.16	39	43	2.2 ± 0.2	4.3E-8 ± 1.3E-8	bcu	TXS 2112+108	false
J2141+1615	136	45.5	1	325.44	16.26	0.7	0.43	32	28	2.9 ± 0.2	9.8E-8 ± 2.6E-8	bcu	87 GB 213814.6+161434	true
J2142−2303	137	64.5	2	325.7	−23.06	0.34	0.25	172	50	2.4 ± 0.2	1.2E-7 ± 2.9E-8	bcu	PMN J2142−2303	false
J2144−3215	138	20.5	1	326.08	−32.26	1.09	1.07	84	26	3.4 ± 0.3	9.2E-8 ± 2.5E-8	fsrq	PKS 2142−319	true

Table B1
(Continued)

1FLT Source Name	SRC NUM	TBIN 1m	Flares	RAJ2000 (deg)	DEJ2000 (deg)	Conf 95 SemiMaj (deg)	Conf 95 SemiMin (deg)	Conf 95 PosAng (deg)	TS	PL Index	Flux (photons cm^{-2} s^{-1})	Class	Assoc Name	Low Conf
J2219−2732	139	96	1	334.99	−27.53	0.41	0.32	113	30	2.6 ± 0.2	5.1E-8 ± 1.5E-8	fsrq	PMN J2219−2719	true
J2241−3550	140	86	2	340.42	−35.84	0.72	0.39	79	31	2.9 ± 0.3	7.6E-8 ± 1.9E-8	bcu	PMN J2241−3559	false
J2302+0457	141	47.5	1	345.53	4.97	0.55	0.46	90	28	2.8 ± 0.3	8.3E-8 ± 2.3E-8	unass		true
J2341−4205	142	86.5	1	355.38	−42.1	0.29	0.23	113	25	2.2 ± 0.3	3.2E-8 ± 1.5E-8	unass		true

Note. Table B1 is published in its entirety in the machine-readable format. This includes all rows and columns reported in the extension SOURCES of the FITS format version of the catalog. A portion is shown here for guidance regarding its form and content.

(This table is available in machine-readable form.)

Table B2
Sun Detection Summary Table

TBIN 1m	RAJ2000 (deg)	DEJ2000 (deg)	repROI	Test Statistic	Flux (photons cm^{-2} s^{-1})	Power-law Index	FLSF Name
0	161.66	7.76	false	30	4.2E-8 ± 1.6E-8	2.2 ± 0.2	···
0	148.65	12.81	true	28	6.2E-8 ± 2.7E-8	2.5 ± 0.3	···
0	135.82	16.92	true	41	6.3E-8 ± 2.1E-8	2.3 ± 0.2	···
0.5	165.39	6.31	false	34	5.4E-8 ± 1.7E-8	2.3 ± 0.2	···
1	165.46	6.38	false	40	5.9E-8 ± 1.7E-8	2.3 ± 0.2	···
5.5	317.67	−16.2	false	33	3E-8 ± 1.2E-8	1.9 ± 0.2	···
6	343.37	−7.18	true	28	7.3E-8 ± 2.3E-8	2.6 ± 0.2	···
6	317.88	−16.2	true	31	3.4E-8 ± 1.5E-8	2.0 ± 0.2	···
7	356.23	−2.04	false	30	1.1E-7 ± 2.7E-8	3.3 ± 0.4	···
11	128.32	18.8	false	28	5.8E-8 ± 2E-8	2.4 ± 0.2	···
11.5	143.8	14.48	false	34	1.0E-7 ± 2.6E-8	3.1 ± 0.3	···
11.5	139.56	15.43	false	30	5.3E-8 ± 1.7E-8	2.4 ± 0.2	···
12	144.14	14.18	false	33	8.5E-8 ± 2.5E-8	2.7 ± 0.3	···
12	139.6	15.46	false	31	5.6E-8 ± 1.7E-8	2.3 ± 0.2	···
13	166.21	5.83	true	31	8.5E-8 ± 2.7E-8	2.5 ± 0.2	···
17	310.77	−18.46	false	33	7E-8 ± 2.3E-8	2.3 ± 0.2	···
18.5	355.84	−1.84	false	29	1.1E-7 ± 3.2E-8	2.9 ± 0.3	···
22.5	110.21	22.15	false	28	5.6E-8 ± 2.4E-8	2.3 ± 0.3	···
23	130.92	18.05	false	25	3.2E-8 ± 2E-8	2.0 ± 0.3	···
23.5	143.92	14.38	false	31	8.4E-7 ± 2.5E-8	2.5 ± 0.2	···
23.5	127.69	19.05	false	35	6.6E-8 ± 2.3E-8	2.3 ± 0.2	···
29	60.69	20.32	false	30	1E-7 ± 2.7E-8	2.8 ± 0.2	···
30.5	347.8	−5.1	false	540	8E-7 ± 5.4E-8	3.1 ± 0.1	2011−03−07
31	347.77	−5.08	false	533	5.9E-7 ± 3.9E-8	3.1 ± 0.1	2011−03−07
31.5	18.16	8.61	false	29	1E-7 ± 2.9E-8	2.8 ± 0.2	···
33.5	75.27	22.49	false	37	2E-7 ± 4.2E-8	3.4 ± 0.3	2011−06−07
35	134.3	16.51	true	30	1E-7 ± 2.5E-8	3.1 ± 0.3	2011−08−04
35	133.49	17.77	true	32	1E-7 ± 2.6E-8	3.1 ± 0.3	2011−08−04
36.5	165.03	6.51	false	1649	1.1E-6 ± 4.7E-8	2.9 ± 0.1	2011−09−06
37	167.86	5.43	true	39	7.5E-8 ± 2.4E-8	2.3 ± 0.3	···
37	165.04	6.49	false	1685	1.1E-6 ± 5.5E-8	2.9 ± 0.1	2011−09−06
41	304.7	−19.37	true	263	5.7E-7 ± 4.8E-8	3.5 ± 0.1	2012−01−23
41.5	304.25	−19.52	false	261	5.7E-7 ± 4.8E-8	3.5 ± 0.1	2012−01−23
42	347.92	−5.06	false	161920	2.2E-5 ± 1.7E-7	2.8 ± 0.1	2012−03−05
42.5	347.91	−5.0	false	74014	2.2E-5 ± 1.8E-7	2.8 ± 0.1	2012−03−07
43	347.91	−5.0	false	168860	2.2E-5 ± 1.7E-7	2.8 ± 0.1	2012−03−07
46.5	106.04	22.28	true	178	3E-7 ± 3.5E-8	3.0 ± 0.1	2012−07−06
54	331.17	−12.05	true	29	8.2E-8 ± 2.3E-8	2.6 ± 0.2	···
56	19.8	8.11	false	160	3.4E-7 ± 3.8E-8	3.2 ± 0.1	2013−04−11
56.5	51.1	18.81	false	949	8.7E-7 ± 4.5E-8	3.1 ± 0.1	2013−05−13a−b
57	51.11	18.83	false	1000	9.8E-7 ± 5E-8	3.2 ± 0.1	2013−05−13a−b
61.5	196.81	−7.11	false	858	9.7E-7 ± 5.2E-8	3.0 ± 0.1	2013−10−11
62	196.84	−7.12	false	812	7E-7 ± 3.8E-8	2.9 ± 0.1	2013−10−11
62	212.8	−13.31	false	26	7.1E-8 ± 2.1E-8	2.6 ± 0.2	2013−10−28c
66	338.18	−9.22	false	8764	6.8E-6 ± 1.2E-7	2.8 ± 0.1	2014−02−25
66.5	338.18	−9.2	false	8560	6.2E-6 ± 1.1E-7	2.8 ± 0.1	2014−02−25
72	155.99	10.14	true	31	9.9E-8 ± 3.5E-8	2.4 ± 0.2	···
72	160.59	8.42	true	2428	3.1E-6 ± 9.5E-8	2.8 ± 0.1	2014−09−01
72.5	160.61	8.37	true	2542	2.6E-6 ± 7.9E-8	2.8 ± 0.1	2014−09−01
90	347.9	−5.41	false	26	5.1E-8 ± 2E-8	2.3 ± 0.3	···
96	161.07	8.21	true	45	4.9E-8 ± 1.7E-8	2.1 ± 0.2	···
96.5	161.13	8.06	true	38	4.8E-8 ± 1.7E-8	2.1 ± 0.2	···
98	218.0	−14.7	true	28	5.8E-8 ± 2E-8	2.2 ± 0.2	···
98.5	218.01	−14.7	false	30	5.2E-8 ± 1.7E-8	2.2 ± 0.2	···
101	315.58	−16.09	true	29	1E-7 ± 2.7E-8	3.0 ± 0.3	···
103.5	0.84	0.33	true	28	3.2E-8 ± 1.6E-8	2.0 ± 0.2	···
104	19.17	8.0	false	37	8.9E-8 ± 2.5E-8	2.6 ± 0.2	···
108.5	165.38	6.33	false	114	4E-7 ± 5E-8	2.9 ± 0.1	2017−09−06a−b
108.5	168.63	4.81	true	19735	7.8E-6 ± 1.1E-7	2.6 ± 0.1	2017−09−10
109	168.61	4.83	true	13639	7.4E-6 ± 1.1E-7	2.6 ± 0.1	2017−09−10

Note. The columns show the detection time bin, the detection localization in equatorial coordinates (J2000), a flag indicating whether the source is detected in overlapping ROIs, the test statistic, the flux with its 1σ uncertainty, the power-law index with its 1σ uncertainty, and the name of the associated solar flare as reported in the first Fermi-LAT solar flare catalog (Ajello et al. 2021)

(This table is available in machine-readable form.)

Table B3
GRB Detection Summary Table

TBIN 1m	RAJ2000 (deg)	DEJ2000 (deg)	repROI	Test Statistic	Energy Flux (MeV cm^{-2} s^{-1})	Flux (photons cm^{-2} s^{-1})	Power-law Index	Trigger	GRB Name
7	90.82	−41.96	false	65	4.4E-5 ± 1.8E-5	4.3E-8 ± 1.5E-8	1.9 ± 0.2	90328401	090328A
7.5	90.69	−41.96	true	50	2.8E-5 ± 1.0E-5	3.9E-8 ± 1.4E-8	2.0 ± 0.2	90328401	090328A
8.5	333.55	−26.58	false	223	6.4E-5 ± 1.2E-5	1.0E-7 ± 1.6E-8	2.1 ± 0.1	90510016	090510A
9	333.52	−26.6	true	168	5.5E-5 ± 1.2E-5	8.6E-8 ± 1.7E-8	2.1 ± 0.1	90510016	090510A
12	264.92	27.35	true	471	1.3E-4 ± 1.9E-5	1.9E-7 ± 2.1E-8	2.1 ± 0.1	90902462	090902B
12.5	264.93	27.33	true	473	1.2E-4 ± 1.7E-5	1.9E-7 ± 2.2E-8	2.1 ± 0.1	90902462	090902B
13	353.52	−66.34	true	251	6.9E-5 ± 1.1E-5	1.5E-7 ± 2.1E-8	2.2 ± 0.1	90926181	090926A
13.5	353.56	−66.35	true	271	7.1E-5 ± 1.0E-5	1.7E-7 ± 2.2E-8	2.3 ± 0.1	90926181	090926A
19.5	192.15	8.74	false	30	2.8E-5 ± 1.6E-5	1.9E-8 ± 1.2E-8	1.8 ± 0.3	100414097	100414A
20	192.17	8.72	true	31	2.8E-5 ± 1.5E-5	2.0E-8 ± 1.0E-8	1.8 ± 0.2	100414097	100414A
46	170.71	8.91	true	61	3.2E-5 ± 5.5E-6	1.3E-7 ± 2.7E-8	2.7 ± 0.2	120624933	120624B
46.5	170.83	8.94	true	60	3.3E-5 ± 5.7E-6	1.4E-7 ± 2.8E-8	2.7 ± 0.2	120624933	120624B
56	173.13	27.71	true	895	2.4E-4 ± 3.6E-5	2.0E-7 ± 1.9E-8	1.9 ± 0.1	130427324	130427A
56.5	173.13	27.72	true	861	2.2E-4 ± 3.0E-5	2.3E-7 ± 2.2E-8	1.9 ± 0.1	130427324	130427A
61	211.99	1.25	true	26	2.1E-5 ± 5.0E-6	1.1E-7 ± 3.1E-8	3.0 ± 0.3	140102887	140102A
62.5	156.67	9.67	false	31	1.8E-5 ± 4.2E-6	6.7E-8 ± 1.9E-8	2.6 ± 0.2	131108862	131108A
63	156.67	9.68	false	47	2.2E-5 ± 4.7E-6	7.6E-8 ± 1.9E-8	2.5 ± 0.2	131108862	131108A
64	10.58	−1.74	false	87	1.1E-4 ± 5.6E-5	4.9E-8 ± 1.8E-8	1.7 ± 0.2	131231198	131231A
64.5	10.57	−1.72	false	71	7.4E-5 ± 4.1E-5	2.4E-8 ± 1.1E-8	1.6 ± 0.2	131231198	131231A
65.5	315.25	−8.73	false	74	4.0E-5 ± 8.3E-6	9.5E-8 ± 2.6E-8	2.3 ± 0.2	140206275	140206B
66	315.26	−8.73	false	71	3.3E-5 ± 6.1E-6	9.1E-8 ± 2.4E-8	2.4 ± 0.2	140206275	140206B
94	308.5	6.92	false	103	4.3E-5 ± 7.9E-6	1.0E-7 ± 2.4E-8	2.3 ± 0.1	160625945	160625B
94.5	308.52	6.93	false	102	4.5E-5 ± 8.4E-6	1.0E-7 ± 2.3E-8	2.2 ± 0.1	160625945	160625B
101.5	256.27	−1.86	true	73	5.0E-5 ± 8.0E-6	1.7E-7 ± 3.6E-8	2.5 ± 0.2	170214649	170214A
102	256.3	−1.78	true	59	4.8E-5 ± 8.0E-6	1.8E-7 ± 3.9E-8	2.6 ± 0.2	170214649	170214A
118.5	0.62	−2.95	true	48	2.2E-5 ± 5.9E-6	4.7E-8 ± 1.4E-8	2.2 ± 0.2	180720598	180720B
119	0.58	−2.92	true	59	3.4E-5 ± 9.3E-6	6.8E-8 ± 1.7E-8	2.2 ± 0.2	180720598	180720B

Note. The columns show the detection time bin, the detection localization in equatorial coordinates (J2000), a flag indicating whether the source is detected in overlapping ROIs, the test statistic, the energy flux with its 1σ uncertainty, the flux with its 1σ uncertainty, the power-law index with its 1σ uncertainty, the GRB trigger number, and the GRB name as reported in Ajello et al. (2019)

(This table is available in machine-readable form.)

Appendix C
Light Curves

The light curves were produced as described in Section 2.4. Figure 17 contains the computed light curves for each 1FLT source. The light curves for sources with SEDs in Figures 11–16 are shown in Section 5; the complete figure set is available in the online journal.

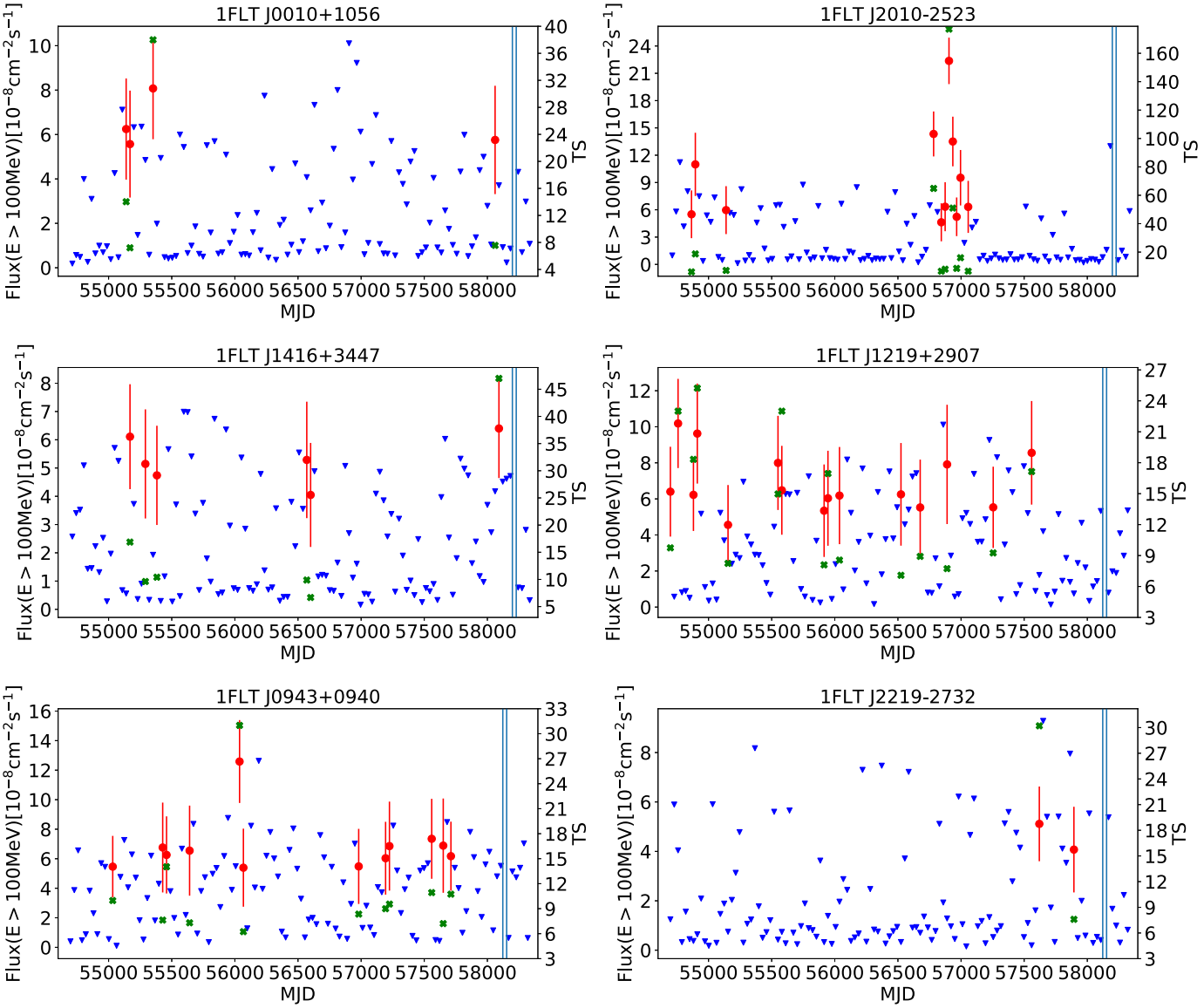

Figure 17. Light curves of sources with SEDs shown in Figures 11–16: red points with error bars represent monthly fluxes with the associated error; blue inverted triangles represent 2σ upper limits (when TS < 4 or $\Delta\mathrm{Flux}/\mathrm{Flux} > 0.5$ or $N_{\mathrm{pred}} < 3$). The green crosses are the value of TS in correspondence of the flux point. The two light-blue lines highlight TBIN 115 (nominal and shifted), which corresponds to a gap in the Fermi-LAT data during the "safe hold" mode in 2018 March when the instrument was powered off. Light curves of sources in the LMC and Cen A regions are not reported, except for 1FLT J0512−7007.

(The complete figure set (138 images) is available.)

ORCID iDs

L. Baldini https://orcid.org/0000-0002-9785-7726
J. Ballet https://orcid.org/0000-0002-8784-2977
D. Bastieri https://orcid.org/0000-0002-6954-8862
J. Becerra Gonzalez https://orcid.org/0000-0002-6729-9022
R. Bellazzini https://orcid.org/0000-0002-2469-7063
E. Bissaldi https://orcid.org/0000-0001-9935-8106
R. D. Blandford https://orcid.org/0000-0002-1854-5506
R. Bonino https://orcid.org/0000-0002-4264-1215
R. A. Cameron https://orcid.org/0000-0003-0942-2747
P. A. Caraveo https://orcid.org/0000-0003-2478-8018
S. Chen https://orcid.org/0000-0003-1586-3653
S. Ciprini https://orcid.org/0000-0002-0712-2479
S. Cutini https://orcid.org/0000-0002-1271-2924
F. D'Ammando https://orcid.org/0000-0001-7618-7527
P. de la Torre Luque https://orcid.org/0000-0002-4150-2539
N. Di Lalla https://orcid.org/0000-0002-7574-1298
L. Di Venere https://orcid.org/0000-0003-0703-824X
A. Domínguez https://orcid.org/0000-0002-3433-4610
A. Fiori https://orcid.org/0000-0003-3174-0688
H. Fleischhack https://orcid.org/0000-0002-5605-2219
Y. Fukazawa https://orcid.org/0000-0002-0921-8837
S. Funk https://orcid.org/0000-0002-2012-0080
P. Fusco https://orcid.org/0000-0002-9383-2425
F. Gargano https://orcid.org/0000-0002-5055-6395
D. Gasparrini https://orcid.org/0000-0002-5064-9495
S. Germani https://orcid.org/0000-0002-2233-6811
N. Giglietto https://orcid.org/0000-0002-9021-2888
F. Giordano https://orcid.org/0000-0002-8657-8852
S. Guiriec https://orcid.org/0000-0001-5780-8770
J. W. Hewitt https://orcid.org/0000-0001-5254-2248
G. Jóhannesson https://orcid.org/0000-0003-1458-7036
M. Kerr https://orcid.org/0000-0002-0893-4073
D. Kocevski https://orcid.org/0000-0001-9201-4706
M. Kuss https://orcid.org/0000-0003-1212-9998
S. Larsson https://orcid.org/0000-0003-0716-107X
L. Latronico https://orcid.org/0000-0002-0984-1856
F. Longo https://orcid.org/0000-0003-2501-2270
F. Loparco https://orcid.org/0000-0002-1173-5673
P. Lubrano https://orcid.org/0000-0003-0221-4806
S. Maldera https://orcid.org/0000-0002-0698-4421
A. Manfreda https://orcid.org/0000-0002-0998-4953
M. N. Mazziotta https://orcid.org/0000-0001-9325-4672
I. Mereu https://orcid.org/0000-0003-0219-4534
M. Meyer https://orcid.org/0000-0002-0738-7581
N. Mirabal https://orcid.org/0000-0002-7021-5838
W. Mitthumsiri https://orcid.org/0000-0002-3776-072X
T. Mizuno https://orcid.org/0000-0001-7263-0296
M. E. Monzani https://orcid.org/0000-0002-8254-5308
A. Morselli https://orcid.org/0000-0002-7704-9553
I. V. Moskalenko https://orcid.org/0000-0001-6141-458X
M. Negro https://orcid.org/0000-0002-6548-5622
V. Paliya https://orcid.org/0000-0001-7774-5308
M. Persic https://orcid.org/0000-0003-1853-4900
M. Pesce-Rollins https://orcid.org/0000-0003-1790-8018
V. Petrosian https://orcid.org/0000-0002-2670-8942
H. Poon https://orcid.org/0000-0002-6004-4270
T. A. Porter https://orcid.org/0000-0002-2621-4440
J. L. Racusin https://orcid.org/0000-0002-4744-9898
S. Rainò https://orcid.org/0000-0002-9181-0345
R. Rando https://orcid.org/0000-0001-6992-818X
B. Rani https://orcid.org/0000-0001-5711-084X
M. Razzano https://orcid.org/0000-0003-4825-1629
S. Razzaque https://orcid.org/0000-0002-0130-2460
A. Reimer https://orcid.org/0000-0001-8604-7077
O. Reimer https://orcid.org/0000-0001-6953-1385
P. M. Saz Parkinson https://orcid.org/0000-0001-6566-1246
D. Serini https://orcid.org/0000-0002-9754-6530
C. Sgrò https://orcid.org/0000-0001-5676-6214
D. J. Suson https://orcid.org/0000-0003-2911-2025
D. Tak https://orcid.org/0000-0002-9852-2469
D. F. Torres https://orcid.org/0000-0002-1522-9065
G. Tosti https://orcid.org/0000-0002-0839-4126
E. Troja https://orcid.org/0000-0002-1869-7817

References

Abdo, A., Ackermann, M., Agudo, I., et al. 2010a, ApJ, 716, 30
Abdo, A., Ackermann, M., Ajello, M., et al. 2010b, ApJ, 710, 810
Abdo, A., Ackermann, M., Ajello, M., et al. 2010c, ApJ, 715, 429
Abdo, A., Ackermann, M., Ajello, M., et al. 2010d, ApJ, 720, 912
Abdo, A., Ackermann, M., Ajello, M., et al. 2010e, ApJ, 722, 520
Abdo, A. A., Ackermann, M., Ajello, M., et al. 2010f, ApJS, 188, 405
Abdollahi, S., Acero, F., Ackermann, M., et al. 2020, ApJS, 247, 33
Abdollahi, S., Ackermann, M., Ajello, M., et al. 2017, ApJ, 846, 34
Abolfathi, B., Aguado, D., Aguilar, G., et al. 2018, ApJS, 235, 42
Acero, F., Ackermann, M., Ajello, M., et al. 2015, ApJS, 218, 23
Ackermann, M., Ajello, M., Albert, A., et al. 2012, ApJS, 203, 4
Ackermann, M., Ajello, M., Albert, A., et al. 2013, ApJ, 771, 57
Ackermann, M., Ajello, M., Albert, A., et al. 2014, Sci, 345, 554
Ackermann, M., Ajello, M., Allafort, A., et al. 2011a, ApJ, 741, 30
Ackermann, M., Ajello, M., Allafort, A., et al. 2011b, ApJ, 743, 171
Ackermann, M., Ajello, M., Atwood, W., et al. 2015, ApJ, 810, 14
Ajello, M., Angioni, R., Axelsson, M., et al. 2020, ApJ, 892, 105
Ajello, M., Arimoto, M., Axelsson, M., et al. 2019, ApJ, 878, 52
Ajello, M., Baldini, L., Bastieri, D., et al. 2021, ApJS, 252, 13
Alam, S., Albareti, F. D., Prieto, C. A., et al. 2015, ApJS, 219, 12
Albareti, F. D., Prieto, C. A., Almeida, A., et al. 2017, ApJS, 233, 25
Angioni, R., Ros, E., Kadler, M., et al. 2020, A&A, 641, A152
Arsioli, B., & Polenta, G. 2018, A&A, 616, A20
Atwood, W., Abdo, A. A., Ackermann, M., et al. 2009, ApJ, 697, 1071
Ballet, J., Burnett, T., Digel, S., & Lott, B. 2020, arXiv:2005.11208
Bednarek, W., Kirk, J. G., & Mastichiadis, A. 1996, A&AS, 120, 571
Best, P., Longair, M., & Röttgering, H. 1997, MNRAS, 292, 758
Bloemen, H., Bennett, K., Blom, J. J., et al. 1995, A&A, 293, L1
Blom, J. J., Bloemen, H., Bennett, K., et al. 1995, A&A, 295, 330
Brandt, C. H. 2018, Master's thesis, ICRANet, Physics Department
Bulgarelli, A., Fioretti, V., Parmiggiani, N., et al. 2019, A&A, 627, A13
Chang, Y.-L., Brandt, C. H., & Giommi, P. 2020, A&C, 30, 100350
Chiang, J. 2012, in Advances in Machine Learning and Data Mining for Astronomy, ed. M. J. Way et al. (Boca Raton, FL: CRC Press), 41
Ciprini, S. & Fermi-LAT Collaboration 2012, in AIP Conf. Ser. 1505, High Energy Gamma-Ray Astronomy: 5th Int. Meeting on High Energy Gamma-Ray Astronomy, ed. F. A. Aharonian, W. Hofmann, & F. M. Rieger (Melville, NY: AIP), 697
Ciprini, S., Tosti, G., Marcucci, F., et al. 2007, in AIP Conf. Proc. 921, The First GLAST Symp. (Melville, NY: AIP), 546
Dallacasa, D., Orienti, M., Fanti, C., Fanti, R., & Stanghellini, C. 2013, MNRAS, 433, 147
Damiani, F., Maggio, A., Micela, G., & Sciortino, S. 1997, ApJ, 483, 370
Fermi LAT Collaboration, Abdo, A. A., Ackermann, M., et al. 2009, Sci, 326, 1512
Giommi, P., Arrigo, G., Barres De Almeida, U., et al. 2020, Space Capacity Building in the XXI Century (Berlin: Springer), 377
Giommi, P., Brandt, C., Barres de Almeida, U., et al. 2019, A&A, 631, A116
Giommi, P., Polenta, G., Lähteenmäki, A., et al. 2012, A&A, 541, A160
Giroletti, M., Giovannini, G., & Taylor, G. B. 2005, A&A, 441, 89
Górski, K. M., Hivon, E., Banday, A. J., et al. 2005, ApJ, 622, 759
Grandi, P., Torresi, E., & Stanghellini, C. 2012, ApJL, 751, L3
Helene, O. 1984, NIMPA, 228, 120
Hewitt, A., & Burbidge, G. 1991, ApJS, 75, 297
Hook, I. M., McMahon, R. G., Shaver, P. A., & Snellen, I. A. 2002, A&A, 391, 509

Jones, D. H., Read, M. A., Saunders, W., et al. 2009, MNRAS, 399, 683
Kolmogorov, A. 1933, Inst. Ital. Attuari, Giorn., 4, 83
Krauß, F., Kreter, M., Müller, C., et al. 2018, A&A, 610, L8
Kreter, M., Gokus, A., Krau, F., et al. 2020, ApJ, 903, 128
Krimm, H. A., Holland, S. T., Corbet, R. H., et al. 2013, ApJS, 209, 14
Laing, R., Riley, J., & Longair, M. 1983, MNRAS, 204, 151
Malizia, A., Landi, R., Molina, M., et al. 2016, MNRAS, 460, 19
Massaro, E., Maselli, A., Leto, C., et al. 2015, Ap&SS, 357, 75
Massaro, F., Masetti, N., D'Abrusco, R., Paggi, A., & Funk, S. 2014, AJ, 148, 66
Mattox, J. R., Bertsch, D., Chiang, J., et al. 1996, ApJ, 461, 396
Migliori, G., Siemiginowska, A., Sobolewska, M., et al. 2016, ApJL, 821, L31
Nolan, P. L., Abdo, A., Ackermann, M., et al. 2012, ApJS, 199, 31
Oh, K., Koss, M., Markwardt, C. B., et al. 2018, ApJS, 235, 4
Paliya, V. S., Koss, M., Trakhtenbrot, B., et al. 2019, ApJ, 881, 154
Planck Collaboration, Ade, P. A. R., Aghanim, N., et al. 2014, A&A, 571, A16
Principe, G., Malyshev, D., Ballet, J., & Funk, S. 2018, A&A, 618, A22
Romero, G. E., Cellone, S. A., & Combi, J. A. 1999, A&AS, 135, 477
Sargent, W. L., & Searle, L. 1970, ApJL, 162, L155
Schilizzi, R. T., Fanti, C., Fanti, R., & Parma, P. 1983, A&A, 126, 412
Schulz, R., Kreikenbohm, A., Kadler, M., et al. 2016, A&A, 588, A146
Sikora, M., Błażejowski, M., Moderski, R., & Madejski, G. 2002, ApJ, 577, 78
Stawarz, L., Ostorero, L., Begelman, M. C., et al. 2008, in ASP Conf. Ser. 386, Extragalactic Jets: Theory and Observation from Radio to Gamma Ray, ed. T. A. Rector & D. S. De Young (San Francisco, CA: ASP), 539
Stawarz, Ł., & Petrosian, V. 2008, ApJ, 681, 1725
Tavani, M., Bulgarelli, A., Vittorini, V., et al. 2011, Sci, 331, 736
Tremblay, S. E., Taylor, G. B., Ortiz, A. A., et al. 2016, MNRAS, 459, 820
Wood, M., Caputo, R., Charles, E., et al. 2017, Proc. ICRC (Busan), 35, 824